

# Wide field aplanatic two-mirror telescopes for ground-based $\gamma$ -ray astronomy

V. Vassiliev<sup>a \*</sup>, S. Fegan<sup>a</sup> and P. Brousseau<sup>a</sup>

<sup>a</sup>Department of Physics & Astronomy, University of California at Los Angeles, Los Angeles, CA, 90095-1562

The field of very high energy (VHE) ground-based  $\gamma$ -ray astronomy, pioneered by the Whipple 10m atmospheric Cherenkov telescope (ACT) [ 1], is being revolutionized by the second generation observatories, H.E.S.S. [ 2], MAGIC [ 3], and VERITAS [ 4]. Dozens of new  $\gamma$ -ray sources, some representing new classes of VHE emitters, have been discovered during the last decade [ 5]. In space based gamma-ray astronomy a leap in technology from SAS-2/COS-B [ 6, 7] to EGRET [ 8] lead to an order of magnitude increase in detected sources; the leap to GLAST/LAT [ 9, 10] technology is anticipated to produce a further order of magnitude increase. The lesson to be learned is that increases in sensitivity, angular resolution and ultimately in scientific output comes through progress in detector technology. In anticipation of such progress it is valuable to re-evaluate the design limitations of current generation ACT observatories and to investigate where improvements can be made that will lead to the next generation. In this paper we focus on one component, the optical system.

## 1. Introduction

ACTs operate in a fundamentally photon starved regime. To avoid contamination of the Cherenkov image with night sky background photons, the exposure must be matched to the intrinsic duration of the Cherenkov light pulse,  $\sim 6$  nsec for an atmospheric cascade. Therefore, unlike in conventional optical astronomy, the image cannot be improved through increased exposure. This motivates the development of optical systems with very large primary mirrors, having diameters in the range of 10–30 m. In addition, the optical systems of ACTs must be composed of the minimal number of optical elements, typically one, to circumvent light loss [ 11, 12, 13, 14]. Thus, to image a Cherenkov light flash with a few nsec exposure, the optical system has to be “ultra-fast”, extending the terminology of photography.

The light detector of an ACT records the individual photons produced as Cherenkov radiation by high energy secondary particles, which are themselves created as a result of the interaction of VHE  $\gamma$ -ray photons and cosmic rays (CRs) with the atmosphere. The atmospheric cascade, which is the physical source of light, develops at the altitude of  $\lesssim 15$  km, and the cascade core has a mean impact distance of a few hundred meters or more

---

\*vzv@astro.ucla.edu

with respect to the telescope position. Therefore, the imaging of Cherenkov radiation from a cascade demands a telescope imaging sensor which accommodates field angles of at least  $1.75^\circ$ . There are several technological motivations to increase the field of view of future ACTs substantially above the minimum of  $3.5^\circ - 4^\circ$ . A larger field of view improves the collecting area of ACTs for the highest energy  $\gamma$ -rays ( $E_\gamma > 10$  TeV), since their cascades can be detected at larger field angles when they impact at a distance of several kilometers [ 15]. Observations of extended sources, such as supernova shells, galactic molecular clouds, or the hot plasma of galaxy clusters, in which  $\gamma$ -rays are produced through interactions of diffuse cosmic rays with ambient matter, would also benefit from increased field of view. At energies below a few hundred GeV the sensitivity of ACTs is limited by the high rate of atmospheric cascades caused by CRs impacting the atmosphere. To accurately estimate this background, and minimize systematic error, it is desirable to contain within the same field of view both the putative source and a few equivalent regions of empty sky. A field of view of  $\sim 10^\circ$  or larger would accommodate observations of galactic and extragalactic extended sources. Finally, the detection of transient VHE phenomena, such as GRBs or rapid AGN flares, provides strong motivation to pursue a future ACT observatory capable of monitoring the full sky with high sensitivity. Currently, observing such transients requires an external trigger from a wide field of view survey instrument, almost exclusively an X-ray satellite with relatively small collecting area. In principle, a large array of ACTs, each having a field of view of  $10^\circ - 15^\circ$ , would be able to provide coverage of  $\sim 1 - 2$  steradians of the sky and generate a self-trigger to initiate more sensitive pointed observations [ 16].

Amongst optical telescopes, ACTs are characterized by an unsurpassed value of étendue (throughput), the volume of the phase space of incoming rays focused by the telescope, equal to the telescope primary mirror area times the field of view solid angle; its typical value for the present day ACTs is  $2 \times 10^3 \text{ m}^2 \text{ deg}^2$ . The UK Schmidt Telescope (UKST) has the largest étendue among existing optical telescopes,  $\sim 60 \text{ m}^2 \text{ deg}^2$ , only 50% larger than that of the Palomar Schmidt,  $\sim 40 \text{ m}^2 \text{ deg}^2$ , built in 1948. The Large Synoptic Survey Telescope (LSST), a state of the art project under consideration, will have étendue of  $\sim 250 \text{ m}^2 \text{ deg}^2$  [ 17]. A future ACT with 12 m diameter primary mirror and  $15^\circ$  field of view would exceed the étendue of LSST by a factor of 80. In view of this comparison, the only reason that ACTs remain relatively inexpensive instruments (the cost of LSST exceeds \$100M) is that these telescopes have low angular resolution; several minutes of arc versus the 0.5 seconds of arc of LSST.

Angular resolution has not been the main parameter driving the design of current generation ACTs and consequently the resolution of their image sensors has been limited to  $\sim 10$  minutes of arc per pixel. At energies larger than a few TeV the sensitivity of ACTs depends weakly on angular resolution, giving little motivation for improvement of this parameter. However, at lower energies ( $< 1$  TeV), the telescope operates in a background dominated regime, and the angular resolution has a major impact on its sensitivity. It has become evident from recent simulation studies that the angular resolution of current generation ACTs is far from the ultimate, dictated by the physics of Cherenkov cascades in the atmosphere [ 18, 16]. To accurately reconstruct the arrival direction of a  $\gamma$ -ray, the core of the atmospheric cascade, created by the secondary electrons and positrons with energies roughly above 100 MeV, must be identified in the shower image. Simulations

show that the transverse angular size of the core is  $\sim 1$  minute of arc. Figure 1 illustrates that the reconstruction of the arrival direction of  $\gamma$ -rays deteriorates slowly when the pixel size of the imaging detector increases from 1 to 2 arc minutes, and more rapidly when the pixel size exceeds 4 minutes of arc. Thus, the optics of future ACTs should facilitate imaging with a pixel size of 1 – 4 arc minutes, a factor of 2 – 9 better than present day instruments such as VERITAS and H.E.S.S. (9 arcmin). For telescopes consisting of a single mirror surface, this requirement translates to optical systems with  $f$ -ratio (ratio of focal length of to primary mirror diameter) in the range 2.5 – 3.0, so that the aberrations are contained within the size of a pixel in the imaging detector. Such optical systems are significantly “slower” than those of current ACTs for which the  $f$ -ratio is 1 – 1.2.

An optical system with both large aperture and large  $f$ -ratio leads unavoidably to a large camera plate scale. For example, a 10 m aperture telescope with  $f = 2.5$  has plate scale of 0.73 cm per arcmin, and the desired resolution of a few arcmin matches well to the size of a few cm diameter photo-multiplier tube (PMT). Existing ACT technology utilizes expensive arrays of  $\sim 10^3$  individual PMTs read out by complex, fast electronics with nsec timing. To improve the image resolution by a factor of  $\sim 3$  and increase the field of view by a similar factor, the number of pixels must increase by two orders of magnitude. Issues of cost, reliability of operation, and the difficulty of maintaining  $10^5$  PMTs may limit the scalability of existing technology to future wide field of view instrumentation. It appears that highly integrated, reliable, and inexpensive imaging sensors will be required to address these problems. The discussion of possible technological solutions, such as multi-anode PMTs, Silicon PMs, image intensifiers, etc., is outside the scope of this paper. However, an important feature of all of these novel photon detecting devices is that their small physical size makes them incompatible with the large plate scale of single mirror optical designs.

In this paper we explore the capabilities of two mirror optical systems for ACTs in an attempt to simultaneously balance the competing requirements of small plate scale, moderate tolerance to aberrations, large field of view and large telescope aperture. We set the scale of the optical system by the choice of the physical size of the pixel in the imaging detector, thereby fixing the physical dimensions of all elements, such as the diameter and focal lengths of the primary and secondary mirrors. This approach permits a direct comparison of the performance of single- and two-mirror optical systems assuming that the same imaging detector is installed in the focal plane of each. Rescaling of the pixel size proportionally changes the dimensions of all optical elements without affecting the conclusions of this study regarding the quality of imaging and the achievable field of view. In addition, we limit the amount of acceptable aberration to the angular size of the pixel, which has been constrained by the physics of atmospheric cascades. Although the smallest structures of the Cherenkov light images corresponds to a pixel size of  $\sim 1$  minute of arc, in this study we consider only  $3'$  pixels giving an improvement of the image resolution by a factor of  $\sim 3$  over present day ACTs. Without this compromise, the number of channels in the camera would exceed one million. With the parameters of the camera fixed we investigate one- and two-mirror optical systems to determine the largest effective light collecting area, given the desirable telescope field of view.

The prescribed plate scale fully determines the focal length of the optical system, therefore we are constrained to consider systems for which the product of the optical system

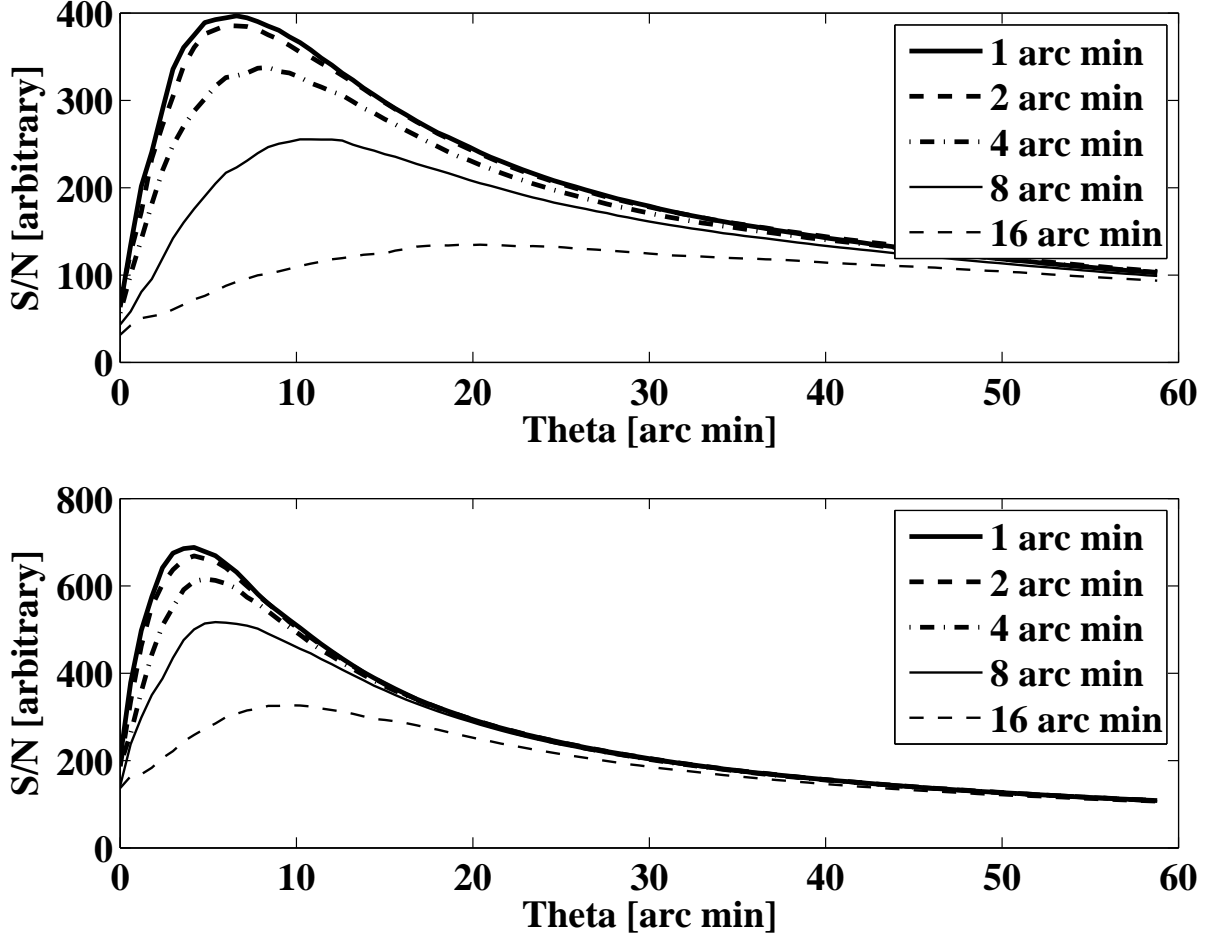


Figure 1. Ratio of the number of  $\gamma$ -ray events reconstructed within angular distance  $\theta$  of the source to the square root of the number of isotropic background events in the same region. The two figures show the results of simulations for 40 and 100 GeV photons. A hypothetical, future generation array of  $75 \text{ m}^2$  telescopes with separation of 80 m and with image sensor quantum efficiency of 25% is assumed [ 16]. The simulations employ the CORSIKA air-shower package [ 19]. To isolate the effect of image sensor pixellation, an idealized telescope model, consisting of two reflective losses with zero dispersion due to PSF, was assumed. The curves show the effects that increasing pixellation in the camera have on the ability of the array to reconstruct the arrival direction of the primary  $\gamma$ -ray. For 1 arc minute pixels the signal-to-background ratio reaches a maximum at approximately 7 and 3.8 minutes of arc from the source location for 40 and 100 GeV photons respectively. With 8 arc minute pixels, slightly smaller than those of current generation instruments such as VERITAS, the ratio reaches a maximum value at approximately 10 and 5 minutes of arc. The relative amplitude of the peaks indicate reduction of the instrument sensitivity by  $\sim 40\%$ .

$f$ -ratio and the primary mirror diameter is constant,  $fD_p = F = \text{const}$ . An increase of the aperture diameter to improve the light-gathering power unavoidably results in a corresponding decrease in the  $f$ -ratio, in turn amplifying all primary aberrations, such as spherical aberration  $\sim 1/f^3$ , coma  $\sim \delta/f^2$ , as well as astigmatism and field curvature  $\sim \delta^2/f$ . We define the “limiting aperture” as the maximal size of the primary mirror for which the optical system produces a high quality image of a point source located at the maximal field angle  $\delta_{\text{max}}$ . For such an optical system, twice the RMS of the point spread function in the tangential or sagittal plane (whichever is the largest),  $2\sigma(\delta_{\text{max}})$ , is equal to the angular size of a pixel in the camera. With a single-mirror optical system it is possible to correct spherical aberrations by using a continuous, parabolic primary or by utilizing the Davies-Cotton design, which has a discontinuous primary mirror. In these systems coma limits the maximal aperture of the telescope. With the two-mirror system, both spherical aberrations and coma can be corrected (Schwarzschild theorem [23]), enabling a further increase of the telescope aperture. One such aplanatic (free of spherical aberrations and coma) Cassegrain system, known as Ritchey-Chrétien [20], is a frequent choice for optical telescopes designed to achieve a high image quality over a large field of view, e.g. the Keck telescopes, VLT, the Hubble Space Telescope, WIYN, etc. In optical telescope applications the secondary mirror is configured to magnify the image and increase the optical system focal length. In contrast, ACTs call for a reduction of the image by the secondary in order to achieve a decreased focal length. The traditional Ritchey-Chrétien configuration of optical telescopes utilizes hyperbolic mirrors for both the primary and secondary to correct first order coma over field angles of a few minutes of arc. The correction of coma over a larger field of view, as required for ACT applications, was investigated by Chrétien in his original works on the Ritchey-Chrétien design [21]. We follow his approach, considering optical systems which correct for coma over a field of view of several degrees by departing from hyperbolic primary and secondary mirror surfaces. In this paper we evaluate the benefits of such an aplanatic telescope (A-T) for ground-based  $\gamma$ -ray astronomy.

The paper is structured as follows. In section 2 we discuss the most traditional single-mirror ACT design, the Davies-Cotton, to establish a benchmark for further comparisons. Section 3 is devoted to the explanation of the A-T optical system. In section 4 we provide the results of ray-tracing simulations performed to determine the optimal parameters for a two-mirror aplanatic telescope. Section 5 contains detailed characteristics of the optical system optimized for application to ground-based gamma-ray astronomy and provides a summary of the results. Throughout this paper we deliberately avoid discussing the advantages and disadvantages of the D-C and A-T optical systems from the perspective of design, fabrication and alignment of the mechanical system and of cost. The latter depends strongly on the specific scientific goals which the instrument must achieve and on the changing costs of different components of the telescope. In the discussion, section 6, we briefly address both subjects.

## 2. Ideal Davies-Cotton telescope

To illustrate the deficiencies of single-mirror telescopes for wide-field imaging applications we review the properties of the Davies-Cotton reflector, which is the most commonly

used design in ground-based  $\gamma$ -ray observatories. Originally, the Davies-Cotton telescope was developed as a solar concentrator [ 24], and as such, it does not satisfy the rigorous requirements of astronomy in the visible wavelength range. Nevertheless, the design has been widely appreciated by  $\gamma$ -ray astronomers for three primary reasons. A large reflector composed of many small, identical, spherical facets is relatively inexpensive to build. The alignment of the optical system is trivial. The performance at large field angles is better than that of a single spherical or parabolic reflector [ 1]. A Davies-Cotton telescope consists of a spherical primary mirror,  $\vec{r}(\varphi, \theta)$ , with radius equal to the focal length of the system,

$$\vec{r}(\varphi, \theta) = F \begin{pmatrix} \sin \theta \cos \varphi \\ \sin \theta \sin \varphi \\ 1 - \cos \theta \end{pmatrix}.$$

The normals of the individual facets,  $\vec{n}$ , are aligned to a single point  $(x, y, z) = (0, 0, 2F)$  so that

$$\vec{n} = \begin{pmatrix} -\sin \frac{\theta}{2} \cos \varphi \\ -\sin \frac{\theta}{2} \sin \varphi \\ \cos \frac{\theta}{2} \end{pmatrix}.$$

Since the normals to the facets do not coincide with the normals of the surface of the reflector, the ideal Davies-Cotton design is discontinuous at every point of the primary mirror and therefore the facet size of an ideal telescope must be equal to zero. The effects of finite facet size, which have been investigated through detailed ray tracing [ 25, 26], degrade the imaging by introducing an additional source of aberrations: the astigmatism of individual facets. We omit these effects, and consider only global aberrations, which are irreducible even in ideal Davies-Cotton optics.

For the purposes of ray-tracing we denote the direction of an incoming photon as

$$\vec{g} = \begin{pmatrix} \sin \delta \\ 0 \\ -\cos \delta \end{pmatrix},$$

where  $\delta$  is the field angle. The direction of the ray reflected from the primary is given by,

$$\vec{s} = \vec{g} - 2\vec{n}(\vec{g}, \vec{n}) = \begin{pmatrix} -\cos \delta \sin \theta \cos \varphi + (1 - (1 - \cos \theta) (\cos \varphi)^2) \sin \delta \\ -\cos \delta \sin \theta \sin \varphi - (1 - \cos \theta) \sin \varphi \cos \varphi \sin \delta \\ \cos \delta \cos \theta + \sin \theta \cos \varphi \sin \delta \end{pmatrix}.$$

The crossing of the focal plane by the reflected ray,

$$\begin{pmatrix} \frac{x}{F} \\ \frac{y}{F} \\ 1 + \frac{1}{4} \frac{F}{F_f} \delta^2 \end{pmatrix} = \begin{pmatrix} \sin \theta \cos \varphi \\ \sin \theta \sin \varphi \\ 1 - \cos \theta \end{pmatrix} + t\vec{s},$$

requires that the parameter  $t$  be given by,

$$t = \frac{\cos \theta}{\cos \delta \cos \theta + \sin \theta \cos \varphi \sin \delta} + \frac{\delta^2 F}{4 F_f \cos \theta} \left( 1 - \delta \left( \frac{\sin \theta}{\cos \theta} \right) \cos \varphi \right) + O(\delta^4).$$

To assess the effect of the field curvature we introduced the  $\frac{1}{4} \frac{F}{F_f} \delta^2$  term, assuming that  $2F_f$  is the radius of the curvature of the focal plane. The formulas are valid to the third order in the field angle. The coordinates of the intersection with the focal plane are given by:

$$\begin{aligned} \frac{x}{F} &= \sin \delta \frac{1 + \left(\frac{1}{\cos \theta} - 1\right) \cos^2 \varphi}{\cos \delta + \frac{\sin \theta}{\cos \theta} \cos \varphi \sin \delta} \\ &+ \frac{\delta^2 F}{4 F_f \cos \theta} \left( -\sin \theta \cos \varphi + \delta \left( 1 + \left(\frac{1}{\cos \theta} - 1\right) \cos^2 \varphi \right) \right), \\ \frac{y}{F} &= \sin \delta \frac{\left(\frac{1}{\cos \theta} - 1\right) (\sin \varphi) (\cos \varphi)}{\cos \delta + \frac{\sin \theta}{\cos \theta} \cos \varphi \sin \delta} \\ &+ \frac{\delta^2 F}{4 F_f \cos \theta} \left( -\sin \theta \sin \varphi + \delta \left(\frac{1}{\cos \theta} - 1\right) (\sin \varphi) (\cos \varphi) \right). \end{aligned}$$

The relevant moments of the light distribution in the focal plane of the telescope are determined by averaging over the reflector aperture,

$$\int_0^{\arcsin(\frac{1}{2f})} \int_0^{2\pi} (\dots) 8f^2 \sin \theta \cos \theta d\theta \frac{d\varphi}{2\pi},$$

where the primary  $f$ -ratio,  $f = \frac{F}{D}$ , is assumed to be much larger than 1/2 (expansion parameter is  $\frac{1}{4f^2}$ ). The position of the image centroid in tangential ( $x$ -axis) and sagittal ( $y$ -axis) coordinates is given by:

$$\begin{aligned} \left\langle \frac{x}{F} \right\rangle &= \delta \left( 1 + \frac{1}{2^5 f^2} \right) + \delta^3 \left( \left( \frac{1}{3} + \frac{1}{4} \frac{F}{F_f} \right) + \frac{1}{2^5 f^2} \left( \frac{7}{3} + \frac{3}{4} \frac{F}{F_f} \right) \right), \\ \left\langle \frac{y}{F} \right\rangle &= 0. \end{aligned}$$

The centered second moments of the light distribution are equal to:

$$\begin{aligned} \left\langle \left( \Delta \frac{x}{F} \right)^2 \right\rangle &= \frac{\delta^2}{2^{10} f^4} \left( 1 - \frac{1}{4f^2} \right) \\ &+ \frac{\delta^4}{2^8 f^2} \left( \left( 4 + \frac{F}{F_f} \right)^2 + \frac{1}{6f^2} \left( 35 + \frac{49}{4} \frac{F}{F_f} + \frac{F^2}{F_f^2} \right) \right), \end{aligned}$$

$$\begin{aligned} \left\langle \left( \Delta \frac{y}{F} \right)^2 \right\rangle &= \frac{\delta^2}{2^{10} f^4} \frac{2}{3} \left( 1 + \frac{3^2}{2^5 f^6} \right) \\ &+ \frac{\delta^4}{2^8 f^2} \left( \frac{F^2}{F_f^2} + \frac{1}{f^2} \left( \frac{1}{4} \frac{F}{F_f} + \frac{1}{6} \frac{F^2}{F_f^2} + \frac{1}{9} \right) \right), \end{aligned}$$

$$\left\langle \left( \Delta \frac{x}{F} \right) \left( \Delta \frac{y}{F} \right) \right\rangle = 0. \tag{1}$$

The contributions from the five primary aberrations can be read from these formulas characterizing the distribution of light on the focal plane. The spherical aberration term,  $\propto 1/f^6$ , is eliminated in the Davies-Cotton reflector design. The coma term,  $\propto \delta^2/f^4$ , is the dominant source of aberrations for all field angles  $\delta < \frac{1}{4f}$ . For a maximal field angle,  $\delta_{\max}$  expressed in degrees, this implies that  $f < \frac{9}{\pi} \left[ \frac{5^\circ}{\delta_{\max}} \right]$  ( $f < 2$  for  $\delta_{\max} > 7.16^\circ$  and  $f < 3$  for  $\delta_{\max} > 4.77^\circ$ ). Coma cannot be corrected by introducing curvature into the image plane. Detailed investigations of various single mirror prime-focus designs for wide field of view IACTs [27] suggest that the Davies-Cotton reflector is among those with the smallest coma. For example, for a continuous parabolic primary the tangential RMS due to coma is a factor of  $\sqrt{2}$  larger,  $\sqrt{2} \frac{1}{25} \frac{\delta}{f^2}$ , while the sagittal RMS is similar to a Davies-Cotton reflector. A continuous spherical primary would add spherical aberrations and increase tangential coma by a factor  $\sqrt{14/3} = 2.16$ . A hyperbolic primary reduces tangential coma, however the sagittal component remains unaffected. Astigmatism, the next aberration term,  $\propto \delta^4/f^2$  (RMS  $\propto \delta^2/f$ ), has the same scaling with  $\delta$  and  $f$  as the effect of field curvature. Either tangential or sagittal astigmatism can be corrected by the proper choice of curved focal plane. For instance, the choice of infinite radius of curvature,  $2F_f \rightarrow \infty$ , eliminates sagittal astigmatism, and the choice of  $2F_f = -\frac{1}{2}F$  cancels tangential astigmatism (the minus indicates that the focal plane is curved towards the primary). If the focal plane has curvature  $2F_f = -F$ , the overall blurring caused by astigmatism is minimized but not completely eliminated. The curvature of the focal plane can also affect distortion, the fifth source of aberration, which arises from the change of the plate scale with field angle ( $\delta^3$  term in  $\langle \frac{x}{F} \rangle$  formula). Although the distortion can be dramatically reduced by the choice  $2F_f = -\frac{3}{2}F$ , in practice the reduction of astigmatism is preferred since distortion can be accounted for through calibration.

We consider wide field of view Davies-Cotton telescopes in which coma is the dominant source of aberration. To contain the image of a point source at  $\delta_{\max}$  within a single pixel of the camera sensor, of size  $p$  minutes of arc, one needs

$$2\sqrt{\left\langle \left( \Delta \frac{x}{F} \right)^2 \right\rangle} = \frac{1}{2^4 f^2} \left[ \frac{\delta_{\max}}{1^\circ} \right] < \frac{1}{60} \left[ \frac{p}{1'} \right],$$

which implies  $f > \frac{5}{2} \sqrt{\left[ \frac{\delta_{\max}}{5^\circ} \right] \left[ \frac{3'}{p} \right]}$ . The diameter of the camera,  $d = \left[ \frac{\delta_{\max}}{5^\circ} \right] \frac{\pi}{18} f D$ , exceeds half of the primary mirror diameter (i.e.  $> 25\%$  obstruction of mirror area) when  $\delta_{\max} > 5^\circ \left[ \frac{18}{5\pi} \right]^{\frac{2}{3}} \left[ \frac{p}{3'} \right]^{\frac{1}{3}}$ . Thus, the Davis-Cotton design appears to be an option for a telescope with wide field of view, not exceeding  $10^\circ - 11^\circ$ , for pixel size  $p$  of  $\sim 3$  minutes of arc. A slightly smaller field of view (by  $\sim 10\%$ ) can also be achieved with the parabolic mirror [27]. However, these designs require an optical system with large  $f$ -ratio ( $\geq 2.5$ ), for which the physical size of the pixels in the detector,  $\frac{p}{1\text{cm}} = \frac{\pi}{3.6} f \left[ \frac{p}{3'} \right] \frac{D}{10\text{m}}$ , must exceed  $\sim 2$  cm for a 10 m mirror aperture. This large plate scale prohibits the use of small, highly integrated image sensors, and appears to leave only the option of using an array of  $\sim 4 \times 10^4 \left[ \frac{\delta_{\max}}{5^\circ} \right]^2 \left[ \frac{3'}{p} \right]^2$  individual PMTs. More cost effective and, perhaps, robust technological solutions, such as multi-anode PMTs with a typical plate scale of 3 – 6 mm per pixel, or even more integrated light sensors such as SiPMs, CMOS, etc., cannot be accommodated

in this design without additional optical elements, such as lenses and light concentrators. This limitation and the desire to break the “10°” field of view limit ( $\delta_{\max} = 5^\circ$ ) motivates our study of two-mirror telescope designs which may address both issues simultaneously. Catadioptric systems, with a large aperture lens in front of the camera, are disfavored for ACT application because the technique depends on the detection of broadband Cherenkov radiation, most of which is concentrated in the blue and UV regions of the spectrum. These systems would suffer from considerable chromatic aberrations, and be subject to significant absorption around 300 nm, which is a characteristic of acrylic or glass Fresnel lenses.

With fixed plate scale,  $\frac{P}{p}$ , the maximal primary mirror radius for which the comatic aberrations at  $\delta_{\max}$  field angle are contained within the size of a single pixel is given by

$$\frac{D}{2} = 1\text{m} \left[ \frac{3.6}{\pi} \right] \left[ \frac{P}{5\text{mm}} \right] \left[ \frac{3'}{p} \right] \sqrt{\left[ \frac{5^\circ}{\delta_{\max}} \right] \left[ \frac{p}{3'} \right]}. \quad (2)$$

The effective mirror area, including obstruction of the primary by the camera, is

$$A_{\text{DCeff}}(\delta_{\max}) = 4.125\text{m}^2 \left[ \frac{P}{5\text{mm}} \right]^2 \left[ \frac{5^\circ}{\delta_{\max}} \right] \left[ \frac{3'}{p} \right] \left( 1 - \frac{1}{4} \left[ \frac{5\pi}{18} \right]^2 \left[ \frac{3'}{p} \right] \left[ \frac{\delta_{\max}}{5^\circ} \right]^3 \right). \quad (3)$$

This analytical result neglects the change of the PSF (equations 1) due to obscuration. However, since the PSF is dominated by rays reflected from the outer regions of the mirror, obscuration of the inner portions by the camera is not expected to modify our conclusion considerably. Equation 3 provides a benchmark to which different telescope configurations with angular pixel size  $p$ , coupled to physical pixels of size  $P$ , can be compared.

### 3. Aplanatic two-mirror telescopes

#### 3.1. Definition of optical elements

The basic geometry of the optical system is illustrated in figure 2. Throughout this section we introduce a number of variables to describe aplanatic two-mirror telescopes. The most important are summarized in table 1.

##### 3.1.1. Primary Mirror

The surface of the primary mirror is given by

$$\vec{r}(\varphi, h) = \begin{pmatrix} h \cos \varphi \\ h \sin \varphi \\ z(h) \end{pmatrix}, \quad (4)$$

where  $\varphi \in [0, 2\pi]$  is the polar angle,  $h \in \left[0, \frac{D_p}{2}\right]$  is the running surface radius,  $D_p$  is the primary mirror diameter, and  $z(h)$  is the sag function, that can be expanded as a Taylor series

$$z = F_p \left( Z_1 \left( \frac{h}{F_p} \right)^2 + Z_2 \left( \frac{h}{F_p} \right)^4 + \dots Z_n \left( \frac{h}{F_p} \right)^{2n} + \dots \right). \quad (5)$$

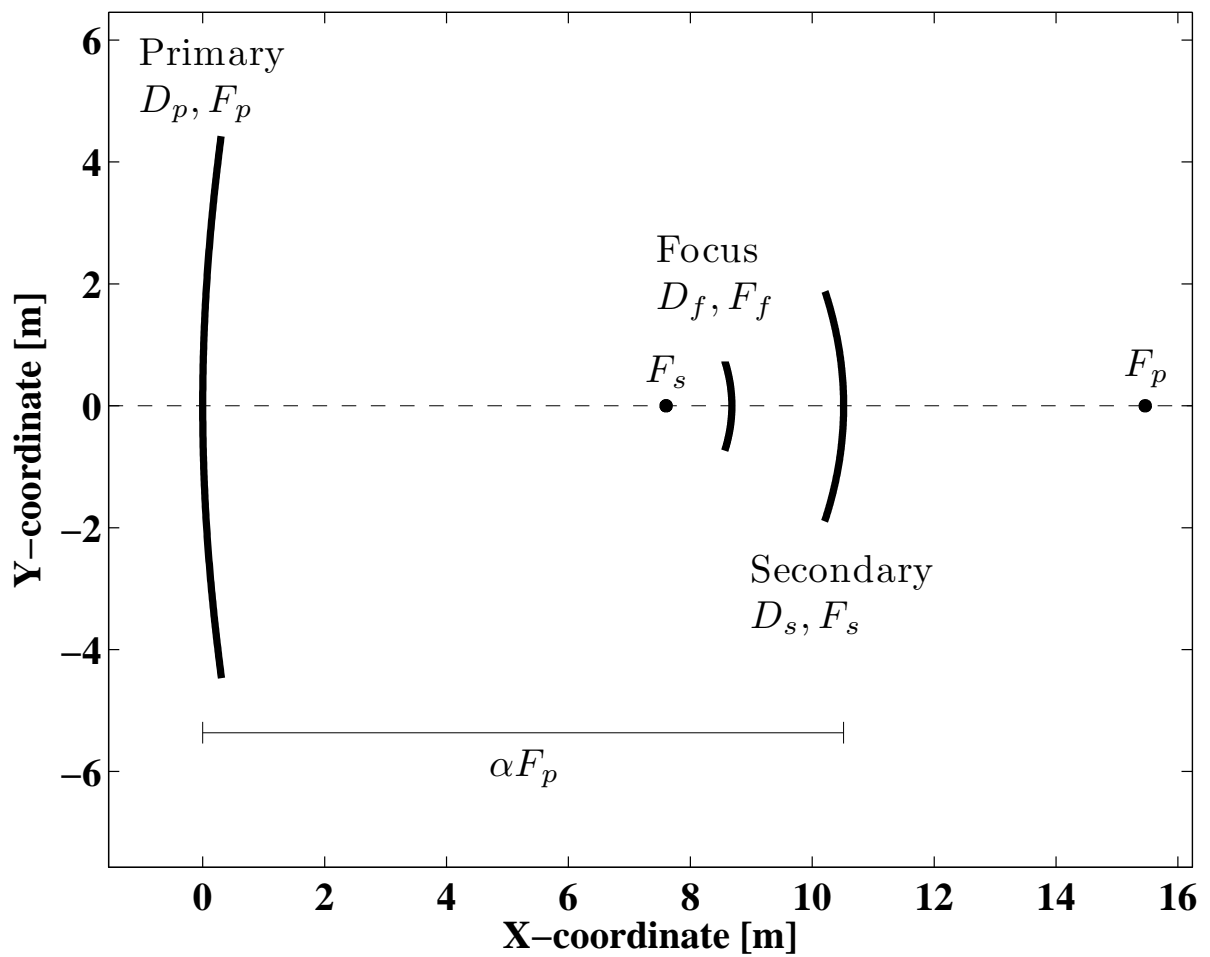


Figure 2. Schematic diagram showing the A-T design and the parameters used to describe the focal lengths and diameters, and placement of the optical elements.

Table 1

Review of variables used in the text.

Variable	Eqn.	Description
$D_p, F_p$	-	Diameter and focal length of primary mirror. See figure 2.
$f_p$	-	f-ratio of the primary $f_p = F_p/D_p$ .
$\varphi$	4	Polar angle on the surface of the primary.
$h$	4	Running radius on the surface of the primary, $h \in [0, D_p/2]$ .
$z(h)$	4	Sag function of the primary.
$z_h$	6	Derivative of primary sag function, $z_h = dz/dh$ .
$D_s, F_s$	-	Diameter and focal length of secondary mirror. See figure 2.
$f_s$	-	f-ratio of the secondary $f_s = F_s/D_s$ .
$\phi$	11	Polar angle on the surface of the secondary.
$\rho$	11	Running radius on the surface of the secondary, $\rho \in [0, D_s/2]$ .
$v(\rho)$	11	Sag function of the secondary.
$v_\rho$	15	Derivative of secondary sag function, $v_\rho = dv/d\rho$ .
$\alpha$	11	Position of the secondary with respect to the primary, in units of the primary focal length. See figure 2.
$D_f, 2F_f$	-	Diameter and focal plane curvature. See figure 2.
$\psi$	16	Polar angle on the focal plane.
$\lambda$	16	Running radius on the surface of the focal plane, $\lambda \in [0, D_f/2]$ .
$f(\lambda)$	16	Field curvature function describing the focal plane.
$P, p$	-	Physical and angular size of a pixel in the camera.
$F$	-	Focal length of the combined optical system.
$1 + \eta$	7	De-magnification due to secondary, relating $F$ and $F_p$ .
$\delta$	-	Field angle, angle of incoming rays with respect to optic axis.
$\delta_{\max}$	-	Maximum field angle, defining field-of-view.
$q = \frac{1}{\alpha(1+\eta)}$	27	Critical parameter of the solution for primary sag function.
$\chi = \frac{1+\eta}{2f_p}$	10,22	Critical parameter of A-T, related to the maximal opening angle of the rays impacting the focal plane.

By convention we choose  $Z_1 = \frac{1}{4}$  so that  $F_p$  is the focal length of the primary mirror. The dimensionless argument  $\frac{h}{F_p}$  runs from zero to  $\frac{1}{2f_p}$ , where  $f_p = \frac{F_p}{D_p}$  is primary mirror  $f$ -ratio. If the primary were chosen to be a conic surface, then the constants  $Z_n$  would be determined as expansion coefficients of

$$2 \frac{1 - \sqrt{1 - \frac{(1+\kappa_p)}{4} x^2}}{(1 + \kappa_p)} = \frac{1}{4} x^2 + \frac{1}{2^6} (1 + \kappa_p) x^4 + \frac{1}{2^9} (1 + \kappa_p)^2 x^6 + \dots$$

In this case, the conic constant  $\kappa_p$  is related to the coefficient  $Z_2$  as  $\kappa_p = 2^6 Z_2 - 1$ , and the remaining aspherical coefficients are determined completely. The normal to the primary surface is

$$\vec{n} = \frac{1}{\sqrt{1 + z_h^2}} \begin{pmatrix} -z_h \cos \varphi \\ -z_h \sin \varphi \\ 1 \end{pmatrix}, \quad (6)$$

where

$$z_h = \frac{dz}{dh} = 2Z_1 \left(\frac{h}{F_p}\right)^1 + 4Z_2 \left(\frac{h}{F_p}\right)^3 + \dots 2nZ_n \left(\frac{h}{F_p}\right)^{2n-1} \dots$$

Assuming the final focal length of the two-mirror telescope is  $F$ , we parametrize the magnification of the secondary mirror by

$$\frac{F}{F_p} = \frac{1}{1 + \eta}, \quad (7)$$

so that the desired image reduction is achieved when  $\eta > 0$ . Since the plate scale is fixed by the given physical and angular pixel size,  $P$  and  $p$  respectively, the primary mirror diameter must satisfy

$$\frac{F_p}{1 + \eta} \left[\frac{p}{3'}\right] \frac{3}{60} \frac{\pi}{180} = D_p \frac{f_p}{1 + \eta} \left[\frac{p}{3'}\right] \frac{\pi}{3.6 \times 10^3} = \left[\frac{P}{5\text{mm}}\right] 5 \times 10^{-3}\text{m},$$

and therefore

$$\frac{D_p}{2} = 5\text{m} \left[\frac{3.6}{\pi}\right] \left[\frac{P}{5\text{mm}}\right] \left[\frac{3'}{p}\right] \left(\frac{1 + \eta}{2f_p}\right). \quad (8)$$

In this definition  $\eta$  and  $f_p$  are free, unit-less parameters of the design and the physical dimensions of all optical elements of the A-T system can be re-scaled by the appropriate choice of  $P$ . In analogy with the Davies-Cotton reflector (equation 3) the effective area of the optical system can be expressed as

$$A_{\text{ATeff}}(\delta_{\text{max}}) = 103.1\text{m}^2 \left[\frac{P}{5\text{mm}}\right]^2 \left[\frac{3'}{p}\right]^2 \left(\frac{1 + \eta}{2f_p}\right)^2 \text{Tr}(f_p, \eta, \delta_{\text{max}}, \dots), \quad (9)$$

where  $\text{Tr}$  is the light transmission coefficient, accounting for obstruction of the primary mirror by the secondary and the secondary mirror by the camera, and for vignetting due to the loss of some oblique rays entering optical system at  $\delta_{\text{max}}$  which miss the secondary

mirror. Section 4 describes the results of numerical simulations of  $A_{\text{ATeff}}(\delta_{\text{max}})$  for various design parameters.

The ratio,

$$\chi = \frac{1 + \eta}{2f_p}, \quad (10)$$

appears frequently in the following calculations and, for this reason, we identify its approximate physical meaning. According to Liouville's theorem étendue is preserved through the optical system. Requiring that the étendue at the primary mirror and at the focal plane be equal,

$$\pi \left( \frac{D_p}{2} \right)^2 \times \pi \left( \frac{\delta_{\text{max}}}{1^\circ} \frac{\pi}{180} \right)^2 \simeq \pi \left( \frac{F_p}{1 + \eta} \frac{\delta_{\text{max}}}{1^\circ} \frac{\pi}{180} \right)^2 \times \pi \left( 2 \sin \frac{\Phi}{2} \right)^2,$$

suggests that this ratio is related to the maximal opening angle,  $2\Phi$ , of the rays impacting focal plane  $\chi = \frac{1+\eta}{2f_p} = 2 \sin \frac{\Phi}{2}$ .

### 3.1.2. Secondary mirror

The surface of the secondary mirror is defined analogously

$$\vec{r}(\phi, \rho) = \begin{pmatrix} \rho \cos \phi \\ \rho \sin \phi \\ v(\rho) \end{pmatrix} + \begin{pmatrix} 0 \\ 0 \\ \alpha F_p \end{pmatrix}, \quad (11)$$

where  $\rho$  is the running surface radius,  $\phi$  is the polar angle,  $v(\rho)$  is the sag, and  $\alpha F_p$  is the primary-secondary separation. Following the traditional Cassegrain design of two-mirror systems, the secondary mirror is placed inside of the primary mirror focus ( $\alpha < 1$ ). However unlike the Cassegrain design, which uses a magnifying, convex secondary mirror, we use a concave reflector to reduce the size of the image. The optically equivalent, Gregorian-like configuration ( $\alpha > 1$ ) with convex secondary mirror is disfavored because it leads to a larger primary-secondary separation and ultimately to a more expensive telescope. Reduction of the image by the secondary mirror, by the factor

$$\frac{F}{F_p} = \frac{1}{1 + \eta} = \frac{F_s}{F_s - (1 - \alpha) F_p}, \quad (12)$$

is achieved with the use of concave secondary with negative focal length,

$$F_s = -\frac{(1 - \alpha) F_p}{\eta}, \quad (13)$$

indicating that it is curved toward the primary. The sag function  $v(\rho)$  can be expanded as

$$v = F_s \left( V_1 \left( \frac{\rho}{F_s} \right)^2 + V_2 \left( \frac{\rho}{F_s} \right)^4 + \dots V_n \left( \frac{\rho}{F_s} \right)^{2n} \dots \right), \quad (14)$$

where  $V_1 = \frac{1}{4}$ . Again, if the secondary is chosen to be a conic surface, its conic constant  $\kappa_s$  would be given by  $\kappa_s = 2^6 V_2 - 1$ . The normal to the secondary mirror is expressed as

$$\vec{s} = \frac{1}{\sqrt{1 + v_\rho^2}} \begin{pmatrix} v_\rho \cos \phi \\ v_\rho \sin \phi \\ -1 \end{pmatrix} \quad (15)$$

where

$$v_\rho = \frac{dv}{d\rho} = 2V_1 \left( \frac{\rho}{F_s} \right)^1 + 4V_2 \left( \frac{\rho}{F_s} \right)^3 + \dots 2nV_n \left( \frac{\rho}{F_s} \right)^{2n-1} + \dots$$

An approximation of the diameter of the secondary mirror is given by

$$D_s \approx D_p \left[ (1 - \alpha) + \alpha f_p \frac{\pi}{18} \frac{\delta_{\max}}{5^\circ} \right].$$

The exact value of  $D_s$  can deviate significantly from this estimate. The diameter of the secondary mirror for zero field ( $\delta_{\max} = 0$ ) is uniquely determined by the configuration of the optical system, through the parameters  $\alpha$  and  $D_p$ . The actual diameter of a practical system, however, may exceed this value and should be determined through optimization in which the effects of obscuration, vignetting, and aberrations are balanced. We discuss this subject further in section 5.

### 3.1.3. Focal Plane

The distance to the focal plane from the secondary mirror  $-\frac{(1-\alpha)}{1+\eta} F_p$  follows from on-axis optical ray tracing. With respect to the primary mirror, the surface of the focal plane is determined by

$$\vec{r}(\psi, \lambda) = \begin{pmatrix} \lambda \cos \psi \\ \lambda \sin \psi \\ f(\lambda) \end{pmatrix} + \begin{pmatrix} 0 \\ 0 \\ \left( \alpha - \frac{(1-\alpha)}{1+\eta} \right) F_p \end{pmatrix}, \quad (16)$$

where  $\lambda$  is the running surface radius,  $\psi$  is the polar angle, and  $f(\lambda)$  is the field curvature function, which can be expressed as a Taylor expansion in the form

$$f = F_f \left( Y_1 \left( \frac{\lambda}{F_f} \right)^2 + Y_2 \left( \frac{\lambda}{F_f} \right)^4 + \dots Y_n \left( \frac{\lambda}{F_f} \right)^{2n} + \dots \right). \quad (17)$$

Again, the parameter  $Y_1 = 1/4$  is chosen by convention. The radius of field curvature,  $2F_f$ , and, if necessary, the high order aspherical terms  $Y_2 = \frac{1}{26} (1 + \kappa_f)$ , etc. should be chosen to minimize astigmatism. In section 4 we describe a numerical optimization which finds the tangential and sagittal focal planes as well as the optimal focal plane, which minimizes the maximal contribution to astigmatism from both projections.

## 3.2. Constraints on the optical system

Assuming that the photon beam is incident on the primary mirror at an angle  $\delta$  in the  $xz$ -plane,

$$\vec{g} = \begin{pmatrix} \sin \delta \\ 0 \\ -\cos \delta \end{pmatrix},$$

the direction of the ray reflected at  $\vec{r}(\varphi, h)$  is given by

$$\vec{g} - 2\vec{n}(\vec{g}, \vec{n}) = \frac{\cos \delta}{z_h^2 + 1} \begin{pmatrix} -2z_h \cos \varphi \\ -2z_h \sin \varphi \\ 1 - z_h^2 \end{pmatrix} + \frac{\sin \delta}{z_h^2 + 1} \begin{pmatrix} 1 - z_h^2 \cos(2\varphi) \\ -z_h^2 \sin(2\varphi) \\ 2z_h \cos \varphi \end{pmatrix}.$$

The intersection of a ray reflected from the primary with the secondary,

$$\begin{pmatrix} h \cos \varphi \\ h \sin \varphi \\ z \end{pmatrix} + t \left[ \begin{pmatrix} -2z_h \cos \varphi \\ -2z_h \sin \varphi \\ 1 - z_h^2 \end{pmatrix} \cos \delta + \begin{pmatrix} 1 - z_h^2 \cos(2\varphi) \\ -z_h^2 \sin(2\varphi) \\ 2z_h \cos \varphi \end{pmatrix} \sin \delta \right] = \begin{pmatrix} \rho \cos \phi \\ \rho \sin \phi \\ v + \alpha F_p \end{pmatrix}, \quad (18)$$

requires that parameter  $t$  be given by

$$t = \frac{\alpha F_p + v - z}{(1 - z_h^2) \cos \delta + 2z_h (\cos \varphi) \sin \delta}.$$

For an on-axis ray ( $\delta = 0$ ) the solution necessitates that  $\varphi = \phi$  and

$$\rho = h - (\alpha F_p + v - z) \frac{2z_h}{1 - z_h^2}. \quad (19)$$

The ray, reflected from the secondary mirror, propagates to the focus of the telescope along a path described by the unit vector

$$\frac{1}{(v_\rho^2 + 1)} \frac{1}{(z_h^2 + 1)} \begin{pmatrix} 2(v_\rho - z_h)(1 + z_h v_\rho) \cos \varphi \\ 2(v_\rho - z_h)(1 + z_h v_\rho) \sin \varphi \\ (v_\rho - z_h)^2 - (1 + z_h v_\rho)^2 \end{pmatrix}.$$

Therefore an optical system which is free from spherical aberrations must satisfy the following requirement,

$$\frac{\rho}{v + \frac{(1-\alpha)}{1+\eta} F_p} = \frac{2(v_\rho - z_h)(1 + z_h v_\rho)}{(v_\rho - z_h)^2 - (1 + z_h v_\rho)^2}. \quad (20)$$

The mathematical conditions for correction of coma can be derived from ray tracing through a perturbative Taylor expansion of equation 18 with respect to  $\delta$ . The deceptively simple ‘‘Abbe sine condition’’, that ensures the exact cancellation of the comatic aberration term in the expansion, requires that the optical system have a particular kind of symmetry. Namely, the intersection points of all rays reaching the focus of the optical system with the incoming rays which produced them (beam parallel to the optical axis) must form spherical surface, i.e.

$$\frac{\rho}{v + \frac{(1-\alpha)}{1+\eta} F_p} = \frac{h}{\sqrt{R^2 - h^2}}. \quad (21)$$

According to equation 19 in the limit of small  $h$ ,

$$\rho = h - (\alpha F_p + v - z) \frac{2z_h}{1 - z_h^2} \approx h - (\alpha F_p) 4Z_1 \frac{h}{F_p} + O(h^2) = (1 - \alpha) h + O(h^2),$$

the radius of the spherical surface can be identified with the focal length of the two-mirror system,

$$R = \frac{1}{1 + \eta} F_p.$$

To satisfy the Abbe sine condition for all running  $h$  from 0 to  $D_p/2$  one needs  $D_p/2 < F_p/(1 + \eta)$ . For a coma free optical system, the reduction of the image by the secondary mirror is therefore limited to

$$\chi = \frac{1 + \eta}{2f_p} < 1. \quad (22)$$

This inequality prohibits the construction of two-mirror systems with arbitrarily small plate scale or alternatively arbitrarily large aperture. As a direct consequence, the telescope imaging camera diameter cannot be made smaller than  $D_p \frac{\pi}{36} \frac{\delta_{\max}}{5^\circ}$ .

The surfaces of both the primary and secondary mirrors of an ideal aplanatic optical system are completely constrained by equations 19, 20, and 21. If we denote

$$G = \frac{1}{\sqrt{1 - \left( (1 + \eta) \frac{h}{F_p} \right)^2}} \text{ and } \sqrt{G^2 - 1} = (1 + \eta) \frac{h}{F_p} G$$

then

$$\rho = \sqrt{G^2 - 1} \frac{(1 - z_h^2) h - 2z_h \left( \left( \alpha - \frac{1-\alpha}{1+\eta} \right) F_p - z \right)}{2z_h + (1 - z_h^2) \sqrt{G^2 - 1}},$$

$$v = \frac{(1 - z_h^2) h (1 - (1 - \alpha) G) - 2z_h (\alpha F_p - z)}{2z_h + (1 - z_h^2) \sqrt{G^2 - 1}},$$

$$v_\rho = \frac{1}{2z_h - (1 - z_h^2) \sqrt{G^2 - 1}} \left( G (1 + z_h^2) - (1 - z_h^2) - 2z_h \sqrt{G^2 - 1} \right).$$

By substituting for the variable  $h$  and re-scaling the sag functions and  $\rho$  one obtains,

$$\sqrt{y} = (1 + \eta) \frac{h}{F_p}, Z = (1 + \eta) \frac{z}{F_p}, z_h = \frac{dz}{dh} = 2\sqrt{y} Z_y, \quad (23)$$

$$\frac{(1 + \eta)}{F_p} \rho = \sqrt{y} \frac{\left( \frac{1}{4} - y Z_y^2 \right) - Z_y \left( (\alpha (1 + \eta) - (1 - \alpha)) - Z \right)}{Z_y \sqrt{1 - y} + \left( \frac{1}{4} - y Z_y^2 \right)}, \quad (24)$$

$$\frac{(1 + \eta)}{F_p} v = \frac{\left( \frac{1}{4} - y Z_y^2 \right) \left( \sqrt{1 - y} - (1 - \alpha) \right) - Z_y \left( \alpha (1 + \eta) - Z \right) \sqrt{1 - y}}{Z_y \sqrt{1 - y} + \left( \frac{1}{4} - y Z_y^2 \right)}, \quad (25)$$

$$v_\rho = \sqrt{y} \frac{\left( \frac{1}{4} \frac{1}{(1 + \sqrt{1 - y})} + (1 + \sqrt{1 - y}) Z_y^2 - Z_y \right)}{Z_y \sqrt{1 - y} - \left( \frac{1}{4} - y Z_y^2 \right)}. \quad (26)$$

These equations can be reduced to a single second order non-linear differential equation for the primary mirror sag function,

$$Z_{yy} = \frac{1}{2} \frac{\left( (\alpha (2 + \eta) - Z - 1) Z_y + y Z_y^2 - \frac{1}{4} \right)}{\left( \alpha (2 + \eta) - Z - 1 + \sqrt{1 - y} \right) \left( 1 - y + \sqrt{1 - y} \right)},$$

which must be solved with the initial conditions  $Z|_{y=0} = 0$  and  $Z_y|_{y=0} = \frac{1}{4} \frac{1}{(1+\eta)}$ . We found that the solution,  $Z(y)$ , has a unique, non-trivial property, which is likely related to the presence of a hidden symmetry in aplanatic optical systems, allowing it to be written

$$Z = \frac{\alpha}{4} qy - (1 - \alpha) \Psi(y, q), \quad (27)$$

where  $q^{-1} = \alpha(1 + \eta)$  and  $\Psi(y, q)$  is a function of only two independent parameters rather than the expected three:  $y$ ,  $\alpha$ , and  $(1 + \eta)$ . This degeneracy requires that  $\Psi$  be a solution of a first order differential equation which can be readily obtained after some mathematical transformations

$$\frac{d\Psi}{dy} = \frac{1}{\sqrt{1-y} - 1 + \frac{2}{q}} \left( \frac{(1 - \Psi)}{(\sqrt{1-y} + 1)} - \frac{1}{2} \right).$$

The solution satisfying  $\Psi|_{y=0} = 0$  and expressed in quadratures is given by

$$\begin{aligned} \Psi(y, q) = & \frac{1}{4} q \frac{y^2}{(\sqrt{1-y} + 1)^2} \left[ \frac{1}{2} - \frac{(q(\sqrt{1-y} - 1) + 2)^{1 + \frac{1}{1-q}}}{(\sqrt{1-y} + 1)^{-1 + \frac{1}{1-q}} (\sqrt{1-y} - 1)^2} \dots \right. \\ & \left. \dots \int_{\sqrt{1-y}}^1 \frac{(2-q)(s-1)^2}{(s+1)^{2 - \frac{1}{1-q}} (q(s-1) + 2)^{2 + \frac{1}{1-q}}} ds \right], \end{aligned}$$

or

$$\Psi(y, q) = 1 - \frac{1}{2} \frac{(q(\sqrt{1-y} - 1) + 2)^{1 + \frac{1}{1-q}}}{(\sqrt{1-y} + 1)^{-1 + \frac{1}{1-q}}} \left( \frac{1}{2} + q \int_0^y \frac{(\sqrt{1-x} + 1)^{-1 + \frac{1}{1-q}}}{(q(\sqrt{1-x} - 1) + 2)^{2 + \frac{1}{1-q}}} dx \right). \quad (28)$$

A non-divergent solution for  $\Psi(y, q)$  exists if

$$\frac{2}{q} = 2\alpha(1 + \eta) > 1 - \sqrt{1 - \chi^2} = \frac{\chi^2}{1 + \sqrt{1 - \chi^2}},$$

or

$$\alpha f_p > \frac{1}{4} \frac{\chi}{1 + \sqrt{1 - \chi^2}}. \quad (29)$$

Analytical solutions can be found for  $q = 1 - \frac{1}{m}$ , where  $m$  is any integer. Simulations indicate that the optimal designs are always found for  $q$  in the range of  $[\frac{1}{2}, \frac{2}{3}]$  and for this reason two boundary solutions have particular importance

$$\Psi(y, q = 1/2) = \frac{1}{32} \frac{y^2}{(1 + \sqrt{1-y})^2} \frac{(1 + 3\sqrt{1-y})}{(1 + \sqrt{1-y})}, \quad (30)$$

$$\Psi(y, q = 2/3) = \frac{1}{162} \frac{y^2}{(\sqrt{1-y} + 1)^2} \frac{(19(1-y) + 28\sqrt{1-y} + 7)}{(\sqrt{1-y} + 1)^2}. \quad (31)$$

For the range of the numerical optimization discussed in the following section, the solution  $\Psi(y, q = 2/3)$  always provides an effective telescope mirror area which is within a few percent from the maximal achievable value.

Within its region of convergence, the general series solution can be represented in the form,

$$\begin{aligned}
\Psi &= \Psi_2 y^2 + \Psi_3 y^3 + \Psi_4 y^4 + \Psi_5 y^5 + \Psi_6 y^6 + \Psi_7 y^7 \\
\Psi_2 &= \frac{1}{32} q \\
\Psi_3 &= \frac{1}{384} q (4 + q) \\
\Psi_4 &= \frac{1}{6144} q (30 + 11q + 2q^2) \\
\Psi_5 &= \frac{1}{122880} q (336 + 146q + 41q^2 + 6q^3) \\
\Psi_6 &= \frac{1}{2949120} q (5040 + 2414q + 829q^2 + 194q^3 + 24q^4) \\
\Psi_7 &= \frac{1}{82575360} q (95040 + 48504q + 18754q^2 + 5489q^3 + 1114q^4 + 120q^5).
\end{aligned} \tag{32}$$

Since

$$\begin{aligned}
Z_1 &= \frac{1}{4} \\
Z_n &= -(1 - \alpha)(1 + \eta)^{2n-1} \Psi_n; n > 1,
\end{aligned}$$

it is evident that the primary mirror is not a conic surface for any choice of  $\alpha$  and  $\eta$ . For the Cassegrain-like design ( $\alpha < 1$ ) the primary is, to first order, a concave hyperbolic mirror in with conic constant  $\kappa_p$  given by  $(1 + \kappa_p) = -2 \left(\frac{1}{\alpha} - 1\right) (1 + \eta)^2$ . However, for all values of  $\alpha$  and  $\eta$  it deviates from a hyperbolic surface in the second expansion order. For the Gregorian-like configuration ( $\alpha > 1$ ) the deviation of the primary from an elliptical surface is also unavoidable for any physical parameters  $\alpha > 0$ , and  $\eta + 1 > 0$ .

The parametric definition of the secondary mirror can be computed numerically based on the equations 23, 24, and 25. We have not been able to derive a general analytic solution representing the mirror surface. The series solution, assuming it is convergent, is given by:

$$\begin{aligned}
\frac{v}{F_s} &= \left( V_1 \left(\frac{\rho}{F_s}\right)^2 + V_2 \left(\frac{\rho}{F_s}\right)^4 + V_3 \left(\frac{\rho}{F_s}\right)^6 + V_4 \left(\frac{\rho}{F_s}\right)^8 + \dots \right) \\
V_1 &= \frac{1}{4} \\
V_2 &= \frac{1}{32} \eta^{-3} (\eta + 1)^2 \left( -2 \frac{\eta}{(\eta+1)} + \frac{1}{\alpha} \right) \\
V_3 &= \frac{1}{384} \eta^{-5} (\eta + 1)^3 \left( 12 \frac{\eta}{(\eta+1)} + \frac{1}{\alpha} (\eta - 11) + \frac{1}{\alpha^2} \right) \\
V_4 &= \frac{1}{6144} \eta^{-7} (\eta + 1)^4 \left( \begin{array}{l} -120 \frac{\eta}{(\eta+1)} - \frac{2}{\alpha} (14\eta + \eta^2 - 77) \\ + \frac{3}{\alpha^2} (5\eta - 3) + \frac{2}{\alpha^3} \end{array} \right) \\
V_5 &= \frac{1}{122880} \eta^{-9} (\eta + 1)^5 \left( \begin{array}{l} 1680 \frac{\eta}{(\eta+1)} \\ + \frac{2}{\alpha} (369\eta + 49\eta^2 + 3\eta^3 - 1357) \\ - \frac{1}{\alpha^2} (778\eta + 29\eta^2 + 189) \\ + \frac{1}{\alpha^3} (61\eta - 19) + \frac{6}{\alpha^4} \end{array} \right) \\
V_6 &= \frac{1}{2949120} \eta^{-11} (\eta + 1)^6 \left( \begin{array}{l} -30240 \frac{\eta}{(\eta+1)} \\ - \frac{12}{\alpha} (1748\eta + 327\eta^2 + 38\eta^3 + 2\eta^4 - 4843) \\ + \frac{10}{\alpha^2} (3258\eta + 219\eta^2 + 5\eta^3 + 1604) \\ + \frac{5}{\alpha^3} (131\eta^2 - 590\eta - 181) \\ + \frac{10}{\alpha^4} (29\eta - 7) + \frac{24}{\alpha^5} \end{array} \right).
\end{aligned} \tag{33}$$

The secondary mirror is also not a conic surface. It can be made to approximate a conic surface in the first and second order by a specific choice of  $\alpha$  and  $\eta$  such that

$$\kappa_s = -\frac{\left(\frac{5}{2}\eta^2 + 7\eta + 5\right)}{\eta^3 + \frac{3}{2}\eta^2} \text{ and } \alpha = \frac{(2\eta + 3)}{(\eta + 1)\eta}.$$

For  $\alpha \in \left[\frac{1}{2}, 1\right]$  this requires that  $\frac{1}{2}(\sqrt{13} + 1) < \eta < \frac{1}{2}(\sqrt{33} + 3)$  and  $-1.704 < \kappa_s < -0.742$ . Numerical optimization suggest that the preferred values of  $\eta$  are in the range  $[1, 2.5]$ , outside of this bound. Thus, like the primary, an optimized secondary mirror deviates from a conic surface in the second order.

#### 4. Numerical ray-tracing simulations

The basic imaging characteristics for various optical system (OS) configurations were obtained through ray-tracing simulations. Each simulated OS has the same plate scale, 5 mm per 3 arc minutes, and therefore the same focal length of 5.73 m, and is characterized by three parameters  $\alpha$ ,  $f_p$ , and  $\chi$ . The shape of the primary mirror was calculated by numerical integration of equation 28 and the surface of the secondary mirror was derived through the parametric representation, equations 23, 24 and 25. This method finds the diameter of the secondary mirror under the zero field approximation. The parameters were varied within the following ranges  $\alpha \in [0.45, 0.85]$ ,  $f_p \in [0.7, 3.2]$ , and  $\chi \in [0.60, 0.98]$ . For each configuration the curvature and the conic constant of the focal plane were numerically computed by minimizing astigmatism. For this purpose, the surfaces of minimal tangential and sagittal astigmatism were determined and the focal plane was defined so that the effective diameter of the PSF,  $\Delta_{\text{psf}} = 2 \times \max\{\text{RMS}_{\text{sagittal}}, \text{RMS}_{\text{tangential}}\}$  is minimized. In the majority of configurations tested the tangential RMS dominates over most of the range of field angles and hence the focal plane is effectively determined by minimizing tangential astigmatism. It is typical that the tangential RMS exceeds the sagittal by 10-15% for field angles larger than 3 degrees. For smaller angles, the sagittal RMS may exceed the tangential slightly, but they are always within a few percent of each other.

With the focal plane resolved, the effective PSF diameter,  $\Delta_{\text{psf}}$ , and the effective light collecting area,  $A_{\text{eff}}$ , were computed as a function of field angle,  $\delta$ , in the range  $\delta \in [0^\circ, 7^\circ]$ . In these calculations, both obscuration by the secondary mirror and by the  $14^\circ$  FoV camera were accounted for. The configuration with the largest  $A_{\text{eff}}$  was determined, subject to the condition that  $\Delta_{\text{psf}}$  at various field angles does not exceed 5, 4, 3, and 2 minutes of arc. It was found that all optimal configurations have  $\alpha f_p \approx 1$  ( $\alpha f_p \in [0.8, 1.2]$ ). For these systems the primary to secondary separation is within 20% of the diameter of the primary mirror. Optical systems with smaller separations are disfavored due to their large obscuration ratio,  $D_s/D_p$ , and those with larger separations suffer from considerable vignetting, since the secondary mirror is not large enough to intercept all oblique rays reflected by the primary. We observed that the performance of the optical systems was not a rapidly varying function of the defining parameters  $\alpha$ ,  $f_p$ , and  $\chi$ . Therefore the bounds on the volume in this three dimensional space which contains the optimal configurations are not strict. Our goal is to narrow the parameter space which needs to be scanned to find optimal solutions. If for the purposes of engineering and implementation, an optical system must deviate slightly from the best configurations, the bounds can be relaxed.

A non-trivial finding is that the parameter  $q = [\alpha(1 + \eta)]^{-1}$ , which was of prime importance in the derivation of the optical surfaces, is constrained to a narrow interval  $q \in [\frac{1}{2}, \frac{2}{3}]$  for all favored solutions. For the majority of these systems  $q$  is closer to the upper bound, therefore the surface of the primary mirror can be described approximately by the analytic solution, equations 27 and 31. Finally, for all optimal configurations the parameter  $\chi$  was found to be within the range  $\chi \in [0.70, 0.97]$ . The larger  $\chi$  values correspond to optical systems with larger primary mirrors, larger  $A_{\text{eff}}$ , but significantly increased  $\Delta_{\text{psf}}$ . In the opposite limit, the point spread function is considerably improved, at the price of decreased effective light collecting area. While analyzing the optimal solutions, a correlation between the  $\chi$  and  $1 + \eta$  parameters was observed, suggesting that their product remains nearly constant,  $2.2 < \chi(1 + \eta) < 2.5$ . This relationship implies that systems with a larger degree of de-magnification at the secondary mirror must have larger  $f_p$ , and consequently smaller primary mirror diameter and smaller opening angle of rays at the focal plane.

The performance of the A-T and D-C designs is compared in figure 3. The left panel shows  $A_{\text{eff}}(\delta_{\text{max}})$  which can be achieved by the designs, if they have the same plate scale and  $\Delta_{\text{psf}}(\delta_{\text{max}})$  is limited to 3 minutes of arc for both. The D-C curve is given by equation 3; the A-T curve is compiled from the characteristics of the best designs ( $\alpha, f_p, \chi$ ) obtained through simulation. It is evident that the decreased aberrations of the aplanatic telescope allows for an increase of  $A_{\text{eff}}(\delta_{\text{max}})$  by a factor larger than 10.

In practice, two effects will reduce the effective light gathering power of the A-T design compared with the single mirror D-C design. First, a fraction of the light will be lost at the second reflection. Current generation ACTs have mirror reflectivity in excess of 80% at 350 nm, even under conditions of extreme weathering. The industrially coated and protected mirrors used in astronomical facilities routinely have reflectivity in excess of 95%. Second, the larger angles at which the photons impact the light detecting sensor in the A-T design, up to  $45^\circ - 50^\circ$ , may introduce light loss. Utilization of anti-reflection technology, such as a thin film of semiconductor deposited on the entrance window, can significantly reduce the reflection coefficient. The large opening angle of the rays impacting the focal plane in an aplanatic telescope may also reduce the efficiency of light concentrators placed in front of the photon sensor. However, the fraction of light lost likely does not exceed 10 – 20%. We discuss this subject further in section 6. These factors combined do not come close to the order of magnitude (or larger) increase in the effective light gathering power of the A-T system.

The effect of vignetting was studied as a final stage of numerical optimization. To extend the diameter of the secondary mirror beyond the zero field approximation, the series solution given by equation 32 and 33 was used. It was found that for the majority of investigated configurations, a series solution for the primary and secondary sag functions with six terms provides a sufficiently accurate description of the mirror surfaces such that  $\Delta_{\text{psf}}(\delta)$  remains unaffected. However, the Taylor series for the optical systems with the largest  $A_{\text{eff}}(\delta)$  converge relatively slowly and the sixth-order series approximation was determined insufficient to reproduce the PSF. For this reason, the numerical solutions obtained directly from the differential equations were fit with sixth-order polynomials and these fits were then used to study vignetting. Increasing the diameter of the secondary mirror reduces  $A_{\text{eff}}(0)$ . For oblique rays,  $\delta \neq 0$ , the total change of  $A_{\text{eff}}(\delta)$  is due to

the combination of two competing effects. Although increasing the obscuration ratio reduces  $A_{\text{eff}}(\delta)$ , the additional rays intercepted by the secondary mirror compensate for this reduction at sufficiently large  $\delta$ . Figure 4 shows that the effective light collecting area can be equalized over a large range of field angles. However, increasing the diameter of the secondary degrades the PSF of the telescope and therefore limits the range of field angles for which a uniform response can be achieved.

Ultimately, the particular configuration appropriate for any application must be determined by balancing the requirements for uniformity of  $A_{\text{eff}}(\delta)$  over a given range of  $\delta$ , maximizing effective area,  $A_{\text{eff}}(0)$ , and minimizing PSF,  $\Delta_{\text{psf}}(\delta)$ . Table 2 shows three configurations tailored to different goals. OS 1 is optimized to achieve the largest effective area, with relaxed requirements for the compensation of vignetting and imaging quality. OS 2 is designed to provide the largest field of view with a uniform response, which is accomplished through a significant reduction in effective light gathering power. For this system the secondary mirror is extended by 25% and the inner region of the primary mirror area is removed. For the design of OS 3, we required both a field of view 14 degrees and an effective PSF diameter of less than three minutes of arc. The performance characteristics of all three systems are shown in figure 5.

## 5. Telescope performance characteristics

A cross-sectional view of OS 2 showing the primary, secondary and focal surfaces is given in figure 6. This figure also illustrates ray tracing for field angles of zero and five degrees. OS 2 provides a compromise between a relatively large effective light gathering area and a large field of view. This configuration is also unique for the degree to which it allows for compensation of vignetting. The coefficients of the primary and secondary mirrors for this configuration are given by

$$Z_i = \{0.25, -0.189377, -0.604706, -4.21374, 21.8275, -425.160\}$$

$$V_i = \{0.25, 0.013625, -0.010453, 0.014241, -0.012213, 0.005184\}.$$

Both the primary and secondary mirrors can be segmented to reduce the cost of the optical system. A possible arrangement of mirror facets, as “petals”, is shown in figure 7. This scheme has the advantage of requiring a minimal number of different surface shapes. A study of the tolerance of alignment and positioning of mirrors is beyond the scope of this paper. Nevertheless, our experience with the simulations suggests that the requirements are stricter than those applied to the H.E.S.S. and VERITAS optical systems. The use of automated alignment and calibration systems will likely be required, e.g. [ 29].

A composite showing the light distribution at different field angles of OS 2 is given in figure 8. The structure in the distribution is shown in more detail for two field angles in figure 9. A considerable distortion is evident in the first figure. As a result of minimizing the astigmatism, the plate scale becomes a slowly varying function of field angle, which is expressed as a cubic term in the mean of the light distribution on the focal plane, as illustrated in section 2. In astronomical telescopes the effect of distortion is removed during the processing of images. For ACTs a similar approach remains valid, although additional care will be required to account for a slightly variable density of night sky

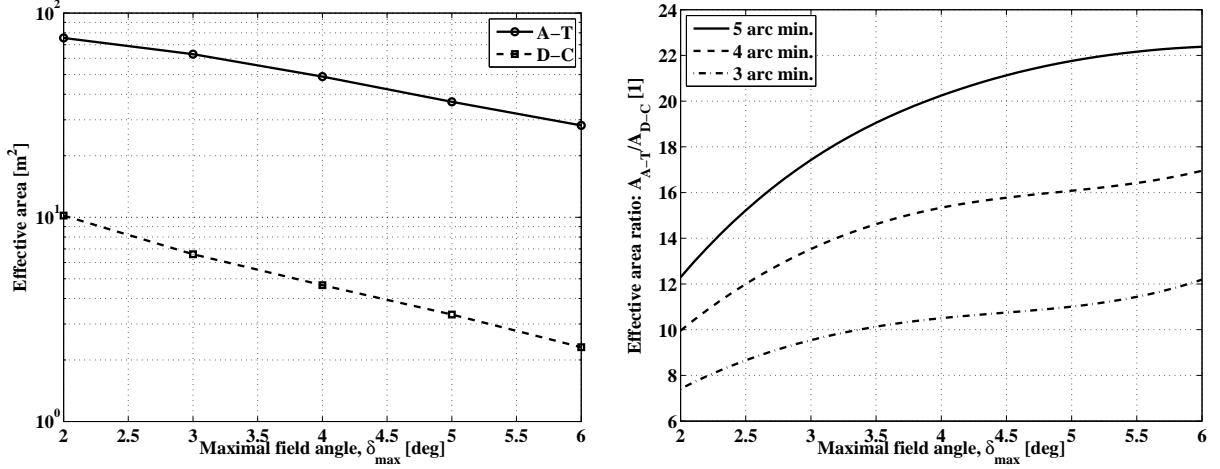


Figure 3. Left: The maximal effective light collecting area of a D-C and an aplanatic telescope, each constrained to have a plate scale of 5 mm per 3 minutes of arc and  $\Delta_{\text{psf}}(\delta_{\max}) < 3'$ . Right: The ratio of  $A_{\text{eff}}(\delta_{\max})$  for aplanatic and D-C telescopes. The three curves correspond to  $\Delta_{\text{psf}}(\delta_{\max})$  constrained to be less than 3, 4, and 5 minutes of arc.

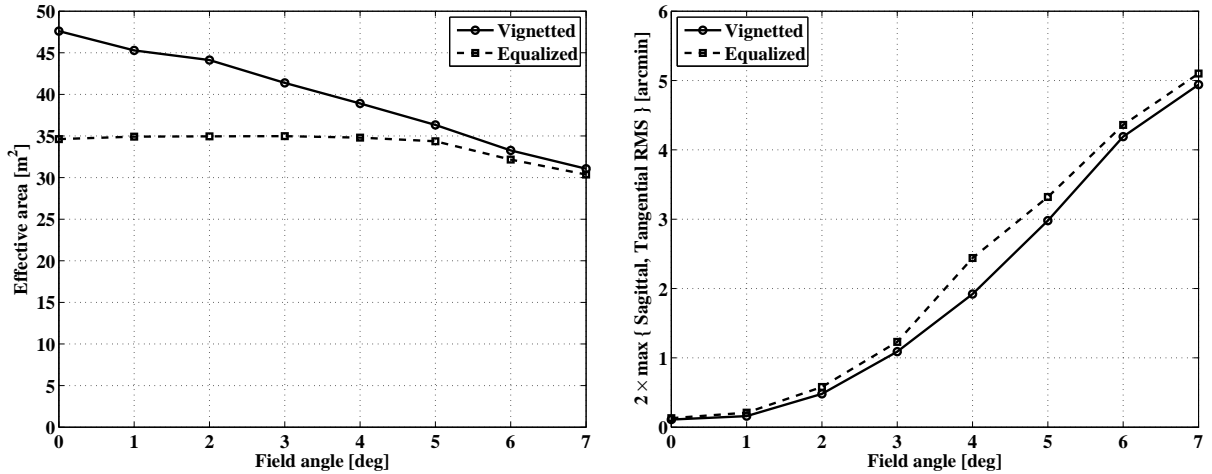


Figure 4. Left: The effective area as a function of field angle for OS 2, table 2. The dashed line shows  $A_{\text{eff}}(\delta)$  when the secondary has been extended by 25% to compensate for vignetting. Right: The effective PSF diameter,  $\Delta_{\text{psf}}(\delta)$ , as a function of field angle. The extension of the secondary mirror of OS 2 successfully equalizes the effective area for field angles up to five degrees with almost no effect on the PSF. This property is not generic for all OSs; normally the secondary mirror can be increased by only  $\sim 10\%$  without significant degradation of imaging.

Table 2

The parameters of three optical systems, tailored for the largest effective area (OS 1), a uniform response over the largest range of field angles (OS 2), and the minimal aberration (OS 3).

Parameters	OS 1	OS 2	OS 3
$D_p$	10.20 m	9.40 m	8.82 m
$D_p$ inner	4.07 m	4.68 m	4.23 m
Primary Mirror Area	68.70 m <sup>2</sup>	52.15 m <sup>2</sup>	47.04 m <sup>2</sup>
$f_p$	1.46	1.80	2.08
$F_p$	14.892 m	16.915 m	18.346 m
$\alpha$	0.66	0.59	0.56
$1 + \eta$	2.599	2.952	3.2032
Secondary Position	9.829 m	9.980 m	10.274 m
$D_s$ (Zerofield)	5.35 m	5.29 m	5.03 m
$D_s$	5.77 m	6.61 m	6.23 m
$D_s$ inner	0.60 m	0.50 m	0.40 m
Secondary Mirror Area	25.87 m <sup>2</sup>	34.12 m <sup>2</sup>	30.36 m <sup>2</sup>
$F_s$	-3.167 m	-3.553 m	-3.664 m
Focal Plane Position	7.881 m	7.631 m	7.754 m
$F_f$	-1.313 m	-1.481 m	-1.479 m
$\kappa_f$	-1.00	-4.28	-6.62
$\Phi = 2 \arcsin \left( \frac{1+\eta}{4f_p} \right)$	52.8°	48.4°	45.3°
Plate Scale	10 cm per deg	10 cm per deg	10 cm per deg
$F$	5.73 m	5.73 m	5.73 m
$A_{\text{eff}}$ (Equalized)	55.26 m <sup>2</sup>	34.92 m <sup>2</sup>	30.54 m <sup>2</sup>
$A_{\text{eff}}$ (Vignetted, Zerofield)	59.85 m <sup>2</sup>	47.61 m <sup>2</sup>	41.24 m <sup>2</sup>
$\Delta_{\text{psf}}$ (5°)	5.60'	3.32'	2.33'

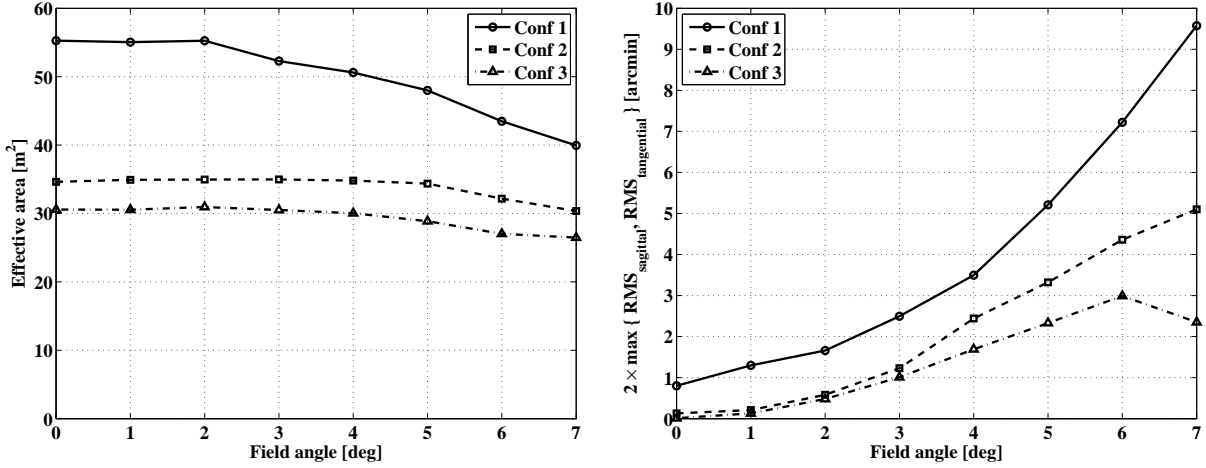


Figure 5. Left: The effective area as a function of field angle for the three configurations of OS summarized in table 2. Right: The effective diameter of the PSF of the light distribution in the focal plane of OSs.

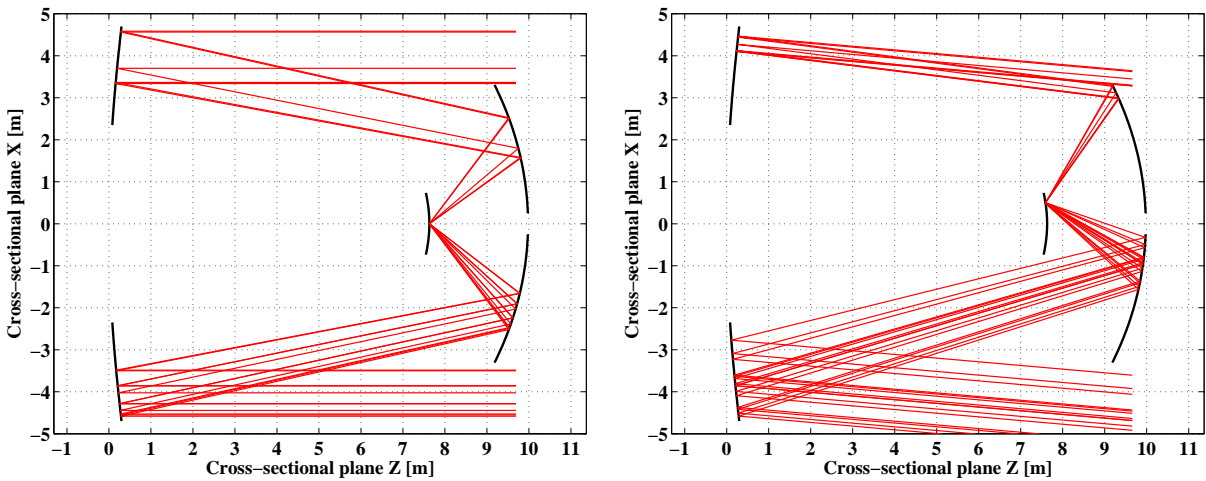


Figure 6. Illustration of incoming rays traced through the optical system to the focal plane for tangential rays at field angles of zero (left) and five (right) degrees.

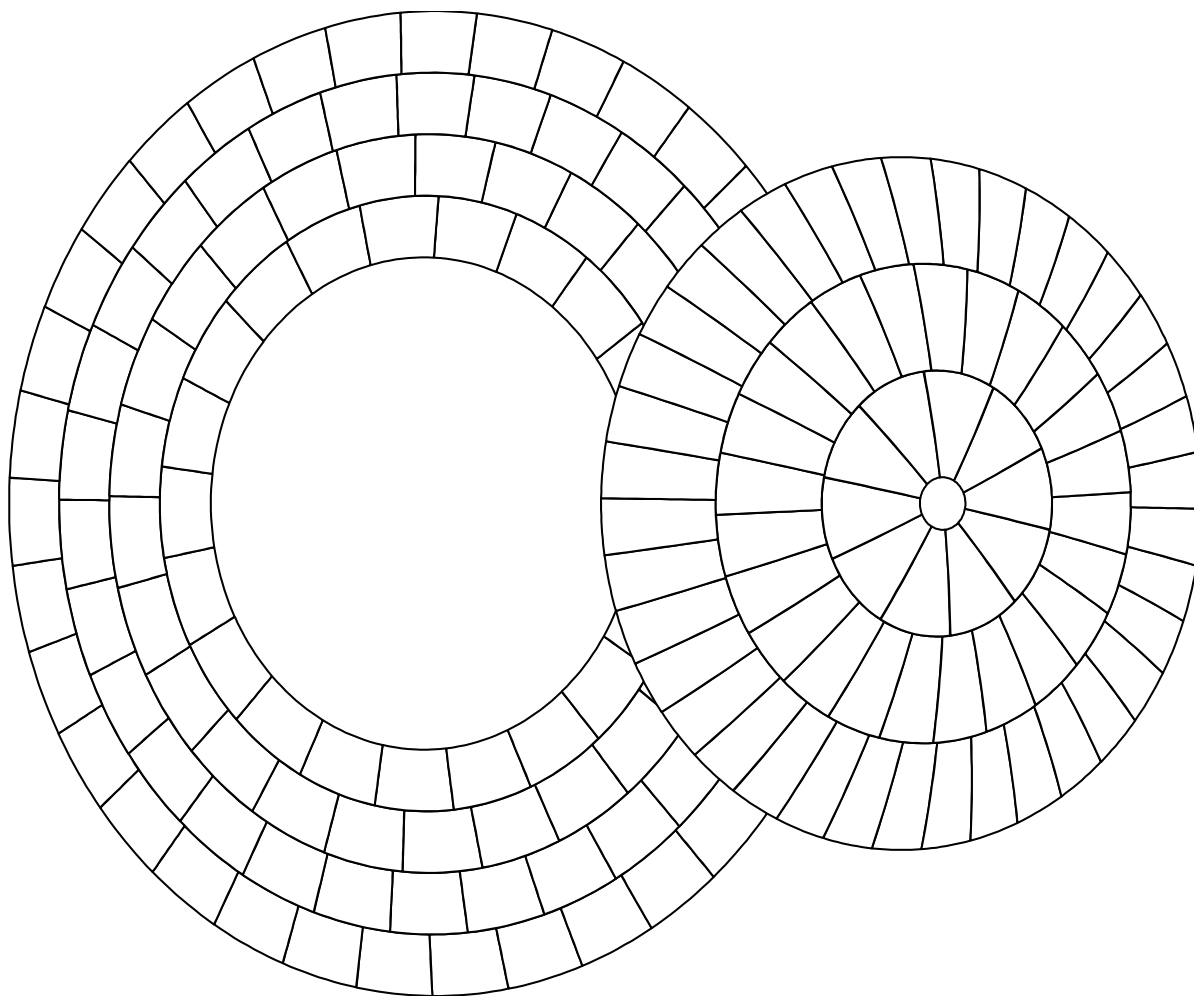


Figure 7. One possible scheme for faceting the primary and secondary mirrors. Four different facet types are used on the primary, three on the secondary. Each facet is limited to an area less than approximately  $0.45 \text{ m}^2$  with no linear dimension larger than 1 m.

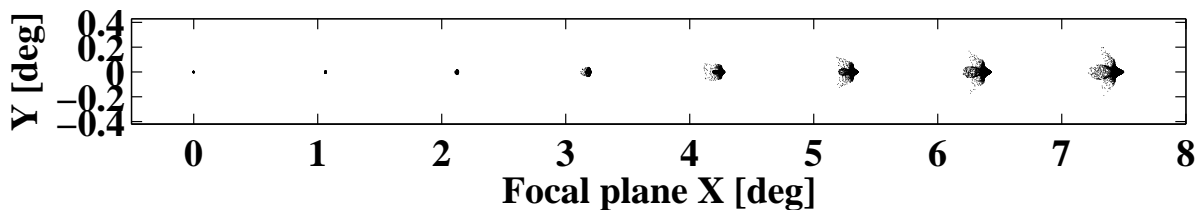


Figure 8. Composite of images made in the focal plane of an aplanatic telescope with configuration OS 2 by rays at field angles between zero and seven degrees.

background photons in the field of view of the telescope. An analogous effect will also be introduced if vignetting is not compensated.

Another characteristic important for ACT applications is the time dispersion introduced by the telescope, which must be less than the intrinsic spread of arrival times of Cherenkov photons (a few nanoseconds). For a D-C telescope, such as VERITAS or H.E.S.S., a planar front incident on the telescope results in an almost uniform spread of the photons at the focal plane, over the interval of 4 – 5 nanoseconds. Such telescopes are not isochronous, even for on-axis photons. The time dispersion increases further for oblique rays and scales linearly with the diameter of the primary mirror. In comparison, the A-T design is isochronous for on-axis rays, and only a small time dispersion is introduced when photons enter the OS at large field angles. Figure 10 shows the results of a simulation of this effect.

## 6. Discussion

We have presented a study of the design of a new, wide-field, two-mirror, aplanatic telescope for ground-based  $\gamma$ -ray astronomy. It has been shown that this design provides a potential alternative to prime-focus optical systems utilized by present-day observatories. If the same plate scale is used in both optical systems, the A-T design radically outperforms the D-C in terms of effective light gathering power, ability to accommodate wide field of view, and amount of time dispersion introduced by the telescope to the arrival times of Cherenkov photons.

Up to field angles of five degrees, both designs offer solution for an optical system with equal light collecting area and an effective PSF diameter smaller than 3 minutes of arc. Although this paper does not present a detailed analysis of the advantages and disadvantages of the mechanical properties of the D-C and A-T designs, some are immediately evident. The D-C design requires a very large focal ratio and photon detector plate scale. Assuming an effective light collecting area of 25 m<sup>2</sup> ( $D_p = 6.2$  m), field of view of 10° ( $\delta_{max} = 5^\circ$ ), and moderate angular pixel size of 5 minutes of arc, one finds that the required focal length is 11.5 m ( $f_p = 1.88$ ). This translates to a camera of diameter of 2 m with 10<sup>4</sup> pixels, each of which must be a 1.8 cm diameter PMT. Such a camera would inevitably have a large mass, and require a sturdy support structure, which would itself present a challenging engineering problem. The lowest fundamental frequencies of the 11.5 m length camera support structure would need to be suppressed to avoid degradation of the optical performance. The moment of inertia of the telescope will likely be dominated by the heavy camera, increasing the time to slew and stabilize the system. However, the clear advantage of the D-C design is the simplicity of the fabrication, assembly and alignment of the reflector.

The A-T design can be made more compact. The equivalent effective light collecting area of 25 m<sup>2</sup> can be achieved with a primary mirror of 7.5 m diameter, after compensating for obscuration effects and loss of light due to the second reflection. The secondary mirror of 4.25 m diameter must be supported at the distance of 7.2 m from the primary. The A-T design allows for rigid support of the camera through the 3 m diameter hole in the primary mirror. The significantly smaller plate scale of the A-T design allows packing of the 10<sup>4</sup> 6 mm pixels within a 75 cm diameter camera. The lowest natural frequencies of the A-T

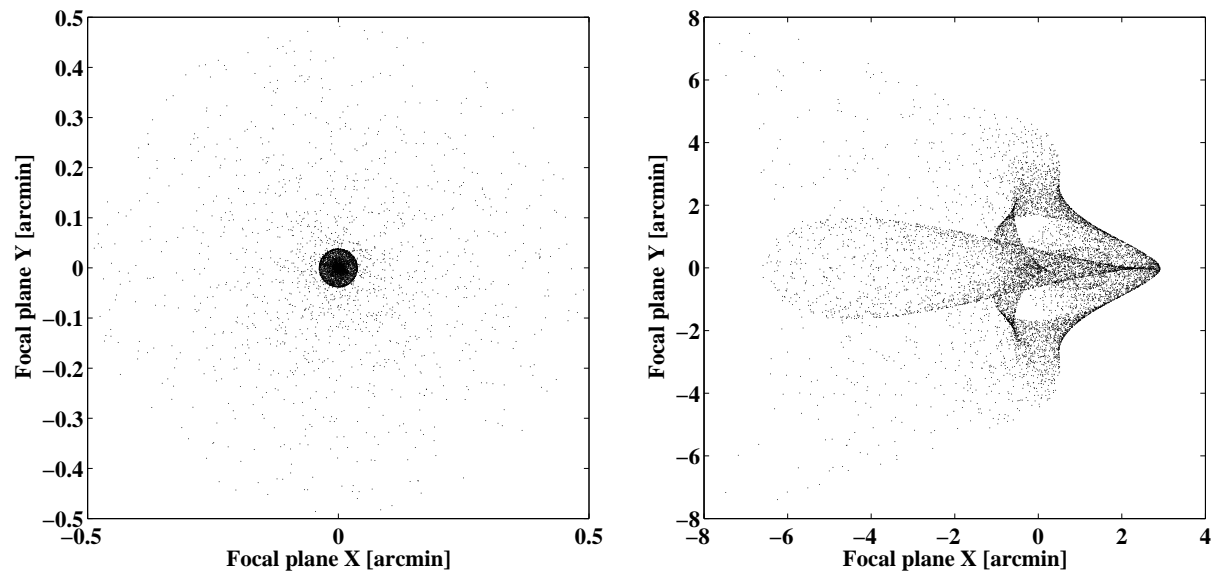


Figure 9. Images made in the focal plane of aplanatic telescope with OS 2 configuration by rays at field angles of zero (left) and five (right) degrees. The origin is chosen at the image centroid.

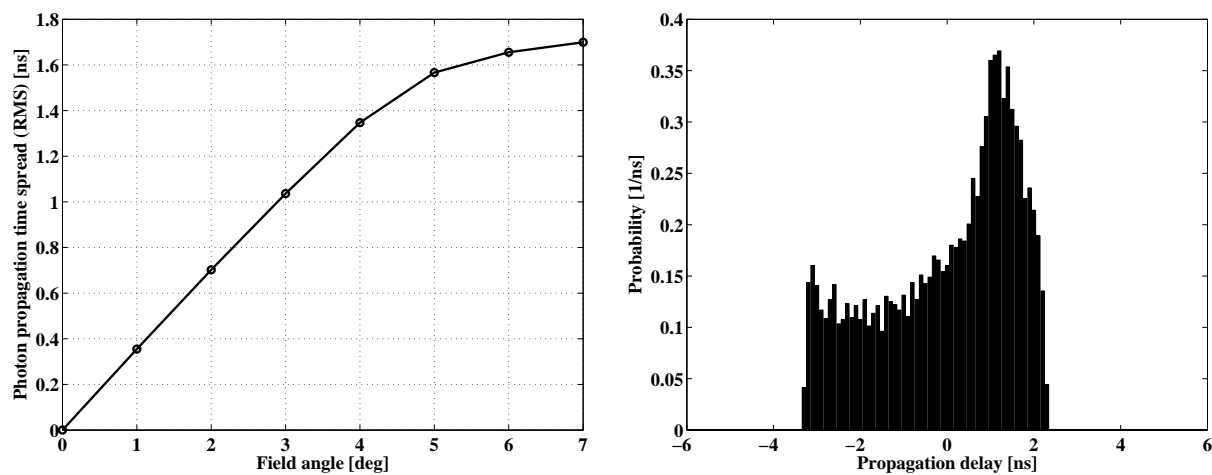


Figure 10. Left: RMS spread in arrival time of rays at the focal plane of aplanatic telescope with OS 2 configuration as a function of field angle. Right: Distribution of arrival times of photons impacting the OS at a field angle of 5 degrees.

optical system are almost twice that of the equivalent D-C configuration. The mass of the primary and secondary mirrors is distributed almost on a spherical surface minimizing moment of inertia. This may allow for fast slewing drive systems and alternative cross-elevation axis mounts. The A-T design allows for a field of view wider than  $\sim 10$  degrees, with pixel size less than 3 minutes of arc, while any prime-focus optical system will suffer from an excessively large obscuration of the primary mirror by the camera. However, the clear disadvantage of A-T is the complexity of the optical system consisting of non-spherical, off-axis mirror elements, challenging mechanical support of the large secondary mirror, and much tighter tolerance requirements for primary and secondary support and alignment. The use of a mirror support structure in which the deflections of the primary and secondary mirrors are matched to maintain correct alignment is likely necessary to overcome the problem of telescope flexure. Such a structure might use the Serrurier truss design, used commonly since the 1930s to mount the primary and secondary mirrors in large optical telescopes, such as the 6.5m MMT and 10m Keck telescopes. The unavoidable need to reduce the OS weight and its moment of inertia will probably require the use of modern, light-weight, high-strength materials, such as carbon fiber-reinforced plastics, to construct the optical support structure. Alignment of the segmented optical system may require automated edge sensors and actuators, since the tolerances of the aplanatic telescope OS are roughly equivalent to a mm range radio telescope, such as ALMA [28], in the range 100–20  $\mu\text{m}$ . Although these requirements are three to four orders of magnitude looser than the diffraction limit to which the positions of the segmented mirrors of the Keck telescopes are maintained, they are far stricter than those of current ACT optical systems, such as VERITAS, MAGIC, and H.E.S.S. Many of the required technological solutions are, however, already being explored by various groups, e.g. [29, 30, 31, 32].

In the traditional D-C design the focal plane is not curved, since the main source of aberration, coma, cannot be corrected by field curvature. The flat imaging camera is assembled from individual PMTs, allowing approximately 75% of the camera to be covered by photon sensitive area (e.g. the 19 mm diameter Hamamatsu R3479, with 15 mm diameter photocathode, arranged in a hexagonal pattern would satisfy the requirements of the D-C telescope described in the example). Light concentrators, typically Winston cones, are used in front of each PMT to collect additional photons from the dead space. The efficiency of light concentrators grows as the opening angle at which photons impact the focal plane is decreased. Collecting efficiencies of  $\sim 50\%$  for dead space photons are routinely achieved by the present day ACTs; higher efficiencies may be possible in optical systems with larger  $f_p$ . Thus for D-C telescopes, light loss at the focal plane can be as small as  $\sim 10\%$ . It is apparent that light concentrators for use on aplanatic telescopes cannot be as efficient, since the full opening angle of rays at the focal plane is large, in the range 90–100 degrees. However, the plate scale of the A-T design is significantly smaller, 6 mm per pixel in the example given, and this allows the use of a more highly integrated light detectors. As an example, the Hamamatsu H8500  $8 \times 8$  MAPMT has a dead space of  $\sim 16\%$ . Light concentrators, though less efficient, can still be used to recover some of the lost photons bringing the difference between the A-T and D-C optical systems to at most a few percent. In fact, small cones can be used in the A-T design to help define the curved focal plane and therefore minimize astigmatism. The use of SiPMs and HPDs, with potentially higher quantum efficiency but significantly larger dead space, may

present a problem. The curved focal plane of the A-T design can be coupled with large aperture electrostatic image intensifiers, since the focal plane is naturally convex, e.g. [33, 34]. In this implementation the dead space is automatically zero, if the photocathode has a uniform quantum efficiency over the full entrance window of the intensifier. For this type of the photodetector the angular resolution of the aplanatic telescope at small field angles is compatible with an image sensor which has an angular pixel size smaller than one minute of arc in the central part of the camera, if desired. It is possible to install a flat camera in the focal plane of an A-T system at the cost of slight degradation of imaging due to increased astigmatism.

Throughout this paper we have intentionally avoided discussing the relative costs of the D-C and A-T designs. Putting aside the fact that the cost of the individual components of ACTs are constantly changing, and that any estimate would be quickly out of date, a meaningful cost comparison can only be made when the instrument design has been decided upon through optimization to address particular scientific goals. For example, one could optimize the instrument to conduct a survey of the largest possible area of sky, at the photon energies around 1TeV, in the shortest amount of time possible to achieve a predetermined sensitivity. Alternatively, one could optimize for the highest sensitivity to point or extended sources at energies above  $\sim 10$  TeV, or to improve the performance in the lowest energy domain. Thus the question of comparison of cost has neither an immediately apparent nor a unique answer.

As an illustration of general considerations of an instrument cost estimation, we examine one possible strategy which could be used to optimize the parameters of a large array of telescopes, for which the footprint of the array is much larger than the characteristic size of the Cherenkov light pool. We also require that the array operates in the background dominated regime. One possible optimization parameter is the total throughput of the observatory, which is the volume of the phase space equal to the effective collecting area for  $\gamma$ -rays times the solid angle of the field of view. With our assumptions, the effective collecting area coincides roughly with the observatory footprint, i.e. the product of the number of telescopes,  $N_t$ , and some characteristic area per telescope,  $A_0$ , determined by the choice of the telescope spacing. The latter is usually selected to balance the desire to increase the baseline for stereoscopic observations, giving a better angular reconstruction of an event, and to decrease it in order to achieve a for higher  $\gamma$ -ray trigger rate, especially at the lowest energies of interest. Thus, the throughput is  $\propto A_0 \times N_t \times \pi \times \delta_{\max}^2$ . We also account for effects of improved angular reconstruction due to the decrease of the detector pixel size,  $p$ , in the optimization parameter. A natural modification is  $T = A_0 \times N_t \times \pi \times \delta_{\max}^2 \times \Lambda^2(p)$ , where  $\Lambda(p)$  expresses the values of the peaks of curves shown in figure 1, relative to the case of  $p = 1$  minute of arc. Optimization of  $T$  is equivalent to the optimization of the sensitivity of the array over its field of view, if the effect of increased pixel size on the efficiency of background rejection is neglected. An expression for the approximate cost of the observatory is  $\$_{total} = N_t \times (\$_{scope} + N_p \times (\$_{pix} + \$_{daq}))$ , where  $\$_{scope}$  is the cost of positioner, optical support and mirrors,  $N_p \simeq \left(\frac{2\delta_{\max}}{p}\right)^2$  is the number of detector pixels per telescope,  $\$_{pix}$  is the cost of the detector per pixel and  $\$_{daq}$  is the average cost of the data acquisition electronics per pixel.

Let us first assume that the cost of the camera dominates the cost of the telescope,

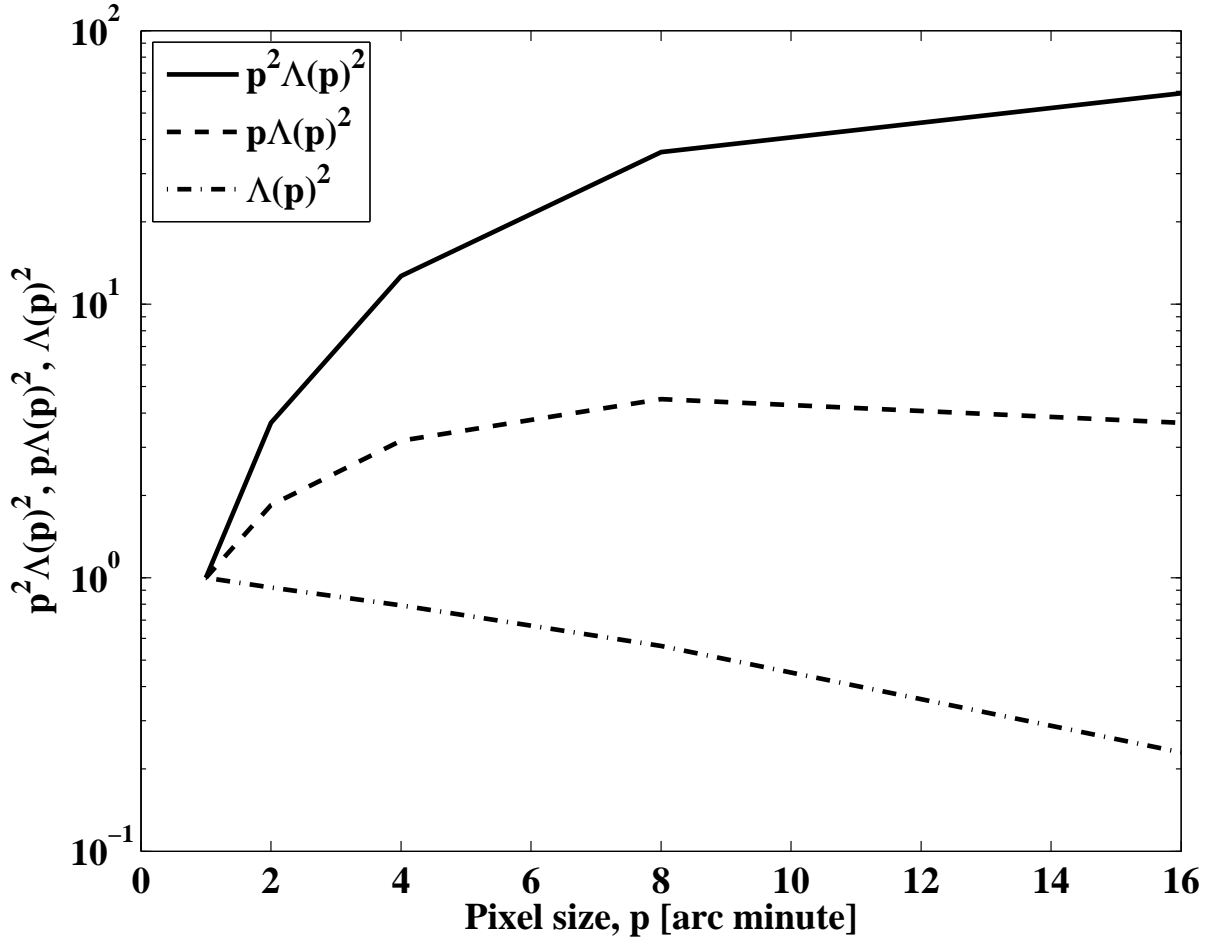


Figure 11. Various expressions involving  $\Lambda(p)$ , the function describing the degradation in the sensitivity of a large array with increased camera pixellation,  $p$ , calculated from figure 1 (100 GeV). The function  $\Lambda(p)$  is normalized with  $\Lambda(1 \text{ arcmin}) = 1$ . The various curves are approximately proportional to the “throughput” of a hypothetical instrument,  $T(p)$ , under different sets of assumptions, as described in the text. The curves obtained for 40 GeV photons show similar trends.

$\$_{scope} \ll N_p \times (\$_{pix} + \$_{daq})$ . Then, with  $N_t \times N_p$  constant to keep the overall cost fixed, the modified throughput,  $T = A_0 \times N_t \times \frac{\pi}{4} \times N_p \times p^2 \Lambda^2(p)$ , is a function of angular pixel size only. Figure 11 shows the behavior of  $p^2 \Lambda^2(p)$  and indicates that the most cost effective strategy is to degrade the angular pixel size to  $p \geq 16$  arc minutes, reducing the number of pixels per camera and degrading the angular resolution of the instrument, while improving the sensitivity due to the increased number of telescopes in the array. This conclusion is a direct consequence of our assumptions, that the array be large compared with the Cherenkov light pool and that it must operate in the background dominated regime, which were in turn required by a specific science goal. A different conclusion follows if observatory footprint is much smaller than its  $\gamma$ -ray collecting area and the array consists of a relatively small number of telescopes. In this case the collecting area and  $T$  scale with  $\sim N_t^{1/2}$  rather than  $N_t$ , and the constraint on overall cost requires that  $p \Lambda^2(p)$  be maximized. The curves shown in figure 11 cannot be used for quantitative conclusions in this limit, since  $\Lambda^2(p)$  was not simulated for an array consisting of a small number of telescopes. Nevertheless, the qualitative trend is evident; the optimal angular pixel size is likely constrained within the interval  $p \in [4, 10]$  minutes of arc.

In the opposite limit,  $\$_{scope} \gg N_p \times (\$_{pix} + \$_{daq})$ , unless the cost of the optical system and positioner is a faster growing function of the PSF diameter,  $\Delta_{psf}(\delta_{max}) = p$ , than  $\Lambda^2(p)$ , the strategy to improve sensitivity through improved angular resolution is preferable. It appears then that under the given assumptions, a cost efficient telescope design requires, roughly, that the cost of the camera doesn't exceed the cost of the optical system and positioner. A design that satisfies this criterion and, at the same time, achieves the ultimate angular resolution of  $\sim 1$  minute of arc might be considered as "perfect". Current ACTs have pixels approximately a factor 8–10 larger than the "perfect" design and technological solutions enabling significant reduction of cost per channel,  $\$_{pix} + \$_{daq}$ , are of great interest.

The A-T design, with significantly smaller plate scale compared to the D-C design of equivalent effective light gathering area, may offer such an opportunity. To illustrate this we use the example discussed above in which D-C and A-T designs require pixels of 1.8 cm and 0.6 cm respectively. The D-C telescope requires that the camera be implemented as an array of PMTs (e.g. Hamamatsu R3479), while the aplanatic telescope can also utilize MAPMT technology (e.g. Hamamatsu H8500). At current prices the per pixel cost of a single PMT exceeds that of a MAPMT by a factor of  $\sim 13$  [35]. The cost of the data acquisition electronics for the A-T design is equal to or less than for the D-C design. Both designs will benefit from the successful application of fast multiplexing, either at the telescope trigger level, which enables only the fraction of the full camera which contains the air-shower image to be digitized and stored, or at the digitization level where optical fiber delay lines are utilized to multiplex signals from several pixels into single FADC channel [36]. These technologies potentially have the promise to reduce  $\$_{daq}$  by a factor of ten or larger. Furthermore, due to the small size of the camera in the example given, 75 cm (29.5 in,  $10^\circ$ ) – 40.6 cm (16 in  $5.4^\circ$ ), the A-T design might be compatible with a camera utilizing a large aperture electrostatic image intensifier and a specialized  $512 \times 512$  or  $1024 \times 1024$  pixel CMOS sensor [37]. Although this technology has not yet matured far enough to offer a practical solution, it promises a substantial reduction in camera cost and a drastic improvement in reliability of camera operation, especially if applied to an

observatory with a large number ( $> 100$ ) of telescopes.

Camera cost can also be decreased through a reduction in field of view, equivalent to a reduction in the number of pixels,  $N_p$ , while keeping the angular pixel size constant. The throughput,  $T$ , is invariant if the field of view is decreased by a factor of two and the number of telescopes is increased by a factor of four. Assuming that the cost of the camera does not dominate the total cost of the telescope, the strategy of increasing the field of view is cost efficient if the optical system and positioner for a single wide field of view instrument can be made less expensive than four instruments of half the field of view. For a modest increase in field of view over the 5 degrees currently utilized by ACTs, it is likely that the D-C design will continue to provide a cost effective strategy. However, a substantial increase in the field of view, and hence in the f-ratio, plate scale and the physical size and weight of the camera, will have a large impact on the cost of a D-C instrument, and may eventually become the dominant factor in the estimation of the total cost of the array. For an aplanatic telescope, a substantial up-front investment will be required for the development of the novel optical system, with its different, aspherical, off-axis mirror elements, which must satisfy the surface shape and alignment tolerances much tighter than presently required for ACT applications. At the same time, the wide-field A-T design potentially offers considerable savings through a dramatically reduced camera cost, and the reduction it allows in the number of optical systems and positioners required to cover the required solid angle in the sky, compared to the narrower field of view D-C telescopes. Evidently, an inexpensive process to manufacture and assemble the segmented optics of the aplanatic telescope is critical to making this design cost effective.

## Acknowledgments

We thank Trevor Weekes and James Buckley for valuable discussions and useful communication and the anonymous referees for their critical remarks and important suggestions, which improved the paper significantly. This material is based upon work supported by the National Science Foundation under Grant No. 0422093.

## REFERENCES

1. Fazio, G., et al., An experiment to search for discrete sources of cosmic gamma rays in the  $10^{11}$  to  $10^{12}$  eV region, *Canadian Journal of Physics*, **46**, 451 (1968)
2. Hofmann, W., Status of the H.E.S.S. project, in *Proc. the 27th International Cosmic Ray Conference, Hamburg, M. Simon, E. Lorenz, M. Pohl (Ed.)*, 2785–2788 (2001)
3. Lorenz, E., Status of the 17 m diameter Magic telescope, in *Proc. the 27th International Cosmic Ray Conference, Hamburg, M. Simon, E. Lorenz, M. Pohl (Ed.)*, 2789–2792 (2001)
4. Weekes, T.C., et al., VERITAS: The Very Energetic Radiation Imaging Telescope Array System, in *Proc. the 25th International Cosmic Ray Conference, Durban, M. Potgieter, C. Raubenheimer, and D. J. van der Walt (Ed.)*, 173 (1997)
5. Ong, R. A., Gamma ray astronomy, c2005 (OG-3), in *Proc. the 29th International Cosmic Ray Conference, Pune, B. Sripathi Acharya, et al. (Ed.)*, **10**, 329–356 (2005)
6. Derdeyn, S. M., et al., SAS-B digitized spark chamber gamma ray telescope, *Nucl. Instr. and Meth.*, **98**, 557 (1972)

7. Bignami, G. F., et al., The COS-B experiment for gamma-ray astronomy, *Space Sci. Instr.*, **1**, 245–268 (1975)
8. Hughes, E. B., et al., Characteristics of the telescope for high energy gamma-ray astronomy selected for definition studies on the Gamma Ray Observatory, *IEEE Transactions on Nuclear Science*, **27**, 364–369 (1980)
9. Atwood, W. B., et al., Gamma Large Area Silicon Telescope (GLAST) applying silicon strip detector technology to the detection of gamma rays in space, *Nucl. Instr. and Meth. A*, **342**, 302–307 (1994)
10. Gehrels, N. and Michelson, P., GLAST: the next-generation high energy gamma-ray astronomy mission, *Astropart. Phys.*, **11**, 277–282 (1999)
11. Bernlöhner, K., et al., The optical system of the H.E.S.S. imaging atmospheric Cherenkov telescopes. Part I: layout and components of the system, *Astropart. Phys.* **20**, 111–128 (2003)
12. Fernandez, J., et al., Optics of the MAGIC telescope, *Appendix A of J. Barrio, et al., The MAGIC Telescope, MPI-PhE/98-5, Max-Planck-Institut für Physik* (1998)
13. Weekes, T. C. et al., VERITAS: the Very Energetic Radiation Imaging Telescope Array System, *Astropart. Phys.* **17**, 221–243 (2002)
14. Kawachi, A., et al., The optical reflector system for the CANGAROO-II imaging atmospheric Cherenkov telescope, *Astropart. Phys.*, **14**, 261–269 (2001)
15. Kifune, T., Takahashi, Y., World wide network for future observations: All sky monitor at VHE energies, in *Proc. Towards a Major Atmospheric Cherenkov Detector V, O. C. de Jager (Ed.), Kruger National Park*, 315–322 (1997)
16. Vassiliev, V., Fegan, S., High Energy All Sky Transient Radiation Observatory, in *Proc. Towards a Major Atmospheric Cherenkov Detector VII, B. Degrange, G. Fontaine (Ed.), Palaiseau*, 445–456 (2005)
17. Tyson, J. A., Large Synoptic Survey Telescope: Overview, Survey and Other Telescope Technologies and Discoveries., in *Proc. the SPIE, J. A. Tyson, S. Wolff (Ed.)* **4836**, 10–20 (2002)
18. Hofmann, W., Performance Limits for Cherenkov Instruments, in *Proc. Towards a Major Atmospheric Cherenkov Detector VII, B. Degrange, G. Fontaine (Ed.), Palaiseau*, 393–400 (2005)
19. Heck, D., et al., CORSIKA: A Monte Carlo Code to Simulate Extensive Air Showers, *Technical report of the Forschungszentrum Karlsruhe, FZKA 6019*, available from [http://www-ik.fzk.de/corsika/physics\\_description/corsika\\_phys.html](http://www-ik.fzk.de/corsika/physics_description/corsika_phys.html) (1998)
20. Schroeder, D.J. (Ed.), *Selected Papers on Astronomical Optics, SPIE Milestone Series*, **MS 73**, SPIE Press (1993)
21. Chrétien, M. H., Le Télescope De Newton Et Le Télescope Aplanétique, *Revue d'Optique Théorique et Instrumentale*, **1**, 13–22 (1922)
22. Wilson, R.N., *Reflecting Telescope Optics I*, Springer-Verlag (1996)
23. Wilson, R.N., *Reflecting Telescope Optics II*, Springer-Verlag (1999)
24. Davies, J. M., Cotton, E. S., Design of the Quartermaster Solar Furnace, *Solar Energy Sci. Eng.*, **1**, 16–22 (1957)
25. Lewis, D. A., Optical characteristics of the Whipple Observatory TeV gamma-ray imaging telescope, *Exp. Astron.*, **1**, 213–236 (1990)
26. Fegan, S. J., Vassiliev, V. V., VERITAS Optics, *VERITAS collaboration internal*

- memo, available from the authors on request (2006)*
27. Schliesser, A., Mirzoyan, R., Wide-field prime-focus imaging atmospheric Cherenkov telescopes: A systematic study, *Astropart.Phys.*, **24**, 382–390 (2005)
  28. Mangum, J. G., et al., Evaluation of the ALMA Prototype Antennas, in *Publications of the Astronomical Society of the Pacific*, **118**, 1260–1304 (2006).
  29. Cornils, R., et al., The optical system of the H.E.S.S. imaging atmospheric Cherenkov telescopes, Part II: mirror alignment and point spread function, *Astropart.Phys.*, **20**, 129–143 (2003)
  30. Garczarczyk M., et al., The Active Mirror Control of the MAGIC Telescope, in *Proc. the 28th International Cosmic Ray Conference, Tsukuba, T. Kajita, et al. (Ed.)*, **5**, 2935-+ (2003)
  31. Mirzoyan, R. and MAGIC Collaboration, Technical Innovations for the MAGIC Project, in *Proc. the 28th International Cosmic Ray Conference, Tsukuba, T. Kajita, et al. (Ed.)*, **5**, 2963-+ (2003)
  32. Cornils, R., et al., The optical system of the H.E.S.S. II telescope, in *Proc. the 29th International Cosmic Ray Conference, Pune, B. Sripathi Acharya, et al. (Ed.)*, **10**, **5**, 171–174 (2005)
  33. Asaoka, Y., et al., Development of a 16-inch UV-Ray Image Intensifier Tube, *IEEE Trans. Nuc. Sci*, **52**, 1773–1778 (2005)
  34. Tada, I. et al., Development of High-Resolution and High-Speed Camera System for a Cherenkov Telescope Using Image Intensifiers, in *Proc. the 28th International Cosmic Ray Conference, Tsukuba, T. Kajita, et al. (Ed.)*, **5**, 2983–2986 (2003)
  35. Hamamatsu corp., private communication (2007)
  36. H. Bartko, H., et al., Tests of a Prototype Multiplexed Fiber-Optic Ultra-fast FADC Data Acquisition System for the MAGIC Telescope *Nucl.Instrum.Meth.*, **A548**, 464–486 (2005)
  37. Tada, I., et al., Detection of Atmospheric Cherenkov Images of Air Showers using High-Resolution and High-Speed Camera System with Image Intensifiers, in *Proc. the 29th International Cosmic Ray Conference, Pune, B. Sripathi Acharya, et al. (Ed.)*, 339-342 (2005)